Control of mitochondrial dynamics by dPGC1 limits Yorkie-induced oncogenic growth in *Drosophila*

Wei Qi Guinevere Sew[1*], Maria Molano-Fernández[1*], Zhiquan Li[2], Artim Lange[1], Nahia Pérez de Ciriza[1], Lene Juel Rasmussen[2] and Héctor Herranz[1]

* These authors contributed equally

[1]Department of Cellular and Molecular Medicine, University of Copenhagen, 2200 Copenhagen N, Denmark

[2]Centre for Healthy Aging, Department of Cellular and Molecular Medicine, University of Copenhagen, 2200 Copenhagen N, Denmark

Correspondence: hherranz@sund.ku.dk

Key words: mitochondria; mitochondrial dynamics; *Drosophila*; Hippo pathway; cancer; cell cycle.

Abstract

Mitochondrial function and dynamics are essential for maintaining cellular homeostasis and overall health. Disruptions in these processes can contribute to various diseases, including cancer. The Hippo signaling pathway, a key regulator of tissue growth, plays a central role in cancer through its main effector, the Yes-associated protein (YAP), known as Yorkie (Yki) in *Drosophila*. In this model organism, *Yki* upregulation drives benign tissue overgrowth in imaginal discs. Our research shows that the conserved metabolic regulator dPGC1 restricts Yki-driven tissue hyperplasia and helps maintain epithelial integrity *in vivo*. Combined *Yki* upregulation and *dPGC1* depletion results in tumors characterized by enlarged mitochondria and upregulation of genes promoting mitochondrial fusion, a condition that is both necessary and sufficient for Yki-driven oncogenic growth. We further demonstrate that mitochondrial enlargement is associated with increased levels of the cell cycle regulator Cyclin E, which is critical for tumor development. These findings identify dPGC1 as a context-dependent tumor suppressor that coordinates mitochondrial dynamics and cell cycle regulation in response to oncogene activation, with implications for understanding cancer development in humans.

Introduction

Cancer is a multistep process that involves the accumulation of mutations affecting different cellular functions known as the hallmarks of cancer. These include central cellular processes such as cell proliferation, apoptosis, and cellular energetics. Together, these hallmarks promote the transformation of normal cells into malignant entities (Hanahan, 2022; Hanahan & Weinberg, 2011). Tumors frequently undergo major changes in their metabolism, which is required to fulfill the high energetic demands of cancer cells. Mitochondria are cytoplasmic organelles that play central roles in cellular energetics. Alterations in mitochondrial function can provide plasticity and adaptability to tumor cells growing in harsh environments, such as hypoxia, reduced nutrient availability, and exposure to cancer treatments (Vyas *et al*, 2016). Consequently, mitochondrial alterations influence various aspects of tumor initiation and disease progression, and genetic changes affecting mitochondria can increase cancer risk (Pavlova & Thompson, 2016; Sullivan *et al*, 2016).

Mitochondria are highly dynamic organelles. Continuous fusion and fission events are crucial for maintaining mitochondrial integrity and function. Mitochondrial fission mediates the division of one mitochondrion into two and is essential for processes such as mitosis and quality control. Mitochondrial fusion, by contrast, merges two mitochondria into one, allowing the exchange of mitochondrial contents and supporting function, especially under cellular stress (Adebayo *et al*, 2021; Mishra & Chan, 2014). Beyond maintaining mitochondrial integrity and function, the balance between fission and fusion is crucial for regulating the cell cycle (Antico Arciuch *et al*, 2012; Qian *et al*, 2012). The cell cycle ensures that a cell replicates and segregates its genome faithfully before it divides into two identical daughter cells. Errors in this process could lead to genomic instability, which is a cancer driver (Tubbs & Nussenzweig, 2017). Defective mitochondrial dynamics can result in an imbalance between fusion and fission, which has been associated with human diseases, including cancer. Therefore, mitochondrial dynamics must be tightly regulated to ensure proper cellular function and tissue homeostasis (Archer, 2013; Dai & Jiang, 2019; Liao *et al*, 2024; Picard *et al*, 2013; Senft & Ronai, 2016; Yu *et al*, 2023).

The Peroxisome Proliferator Activated Receptor Gamma Coactivator-1 (PGC1) family of transcriptional regulators plays central roles in controlling mitochondrial biogenesis and function. This family was originally characterized by the Spiegelman lab, who identified PGC1α as a cold-inducible coactivator of nuclear receptors involved in adaptive thermogenesis and mitochondrial

regulation (Puigserver *et al*, 1998). Subsequent work from the same group demonstrated that PGC1α orchestrates mitochondrial gene expression and respiration (Wu *et al*, 1999), regulates oxidative metabolism and muscle fiber type specification (Lin *et al*, 2002), and promotes mitochondrial biogenesis and oxidative phosphorylation in skeletal muscle cells (Lin *et al*, 2004). In mammals, this family includes PGC1α, PGC1β, and PGC1-related coactivator (PRC) (Scarpulla, 2011; Villena, 2015). These family members share structural and functional similarities. Among them, PGC1α has been most extensively studied in the context of cancer, where it regulates mitochondrial dynamics, metabolic reprogramming, and tumor progression. In contrast, PGC1β and PRC have primarily been characterized in normal physiology, where they regulate mitochondrial biogenesis. While PGC1β and PRC are primarily associated with cellular metabolism and energy homeostasis, PGC1β also contributes to mitochondrial fusion, notably through the regulation of MFN2 and other mitochondrial factors (Liesa *et al*, 2008).

PGC1α controls mitochondrial dynamics by regulating the expression of genes involved in fusion and fission, ensuring a proper balance between these processes to preserve mitochondrial integrity (Abu Shelbayeh *et al*, 2023; Chen *et al*, 2022). The role of PGC1α in cancer is complex and context dependent. It can act both as both a tumor suppressor and as an oncogenic factor, depending on the cancer type and cellular context (Bhalla *et al*, 2011; Girnun, 2012; Jones *et al*, 2012; Tan *et al*, 2016; Torrano *et al*, 2016; Wang *et al*, 2024). Therefore, elucidating the context-specific functions of PGC1α in cancer is crucial for developing targeted therapies. In cancers where PGC1α acts as a tumor suppressor, strategies to enhance its activity might be beneficial. In contrast, in cancers where PGC1α supports tumor growth, inhibiting its function could be a potential therapeutic approach.

Drosophila is emerging as a valuable *in vivo* model to study various aspects of cancer (Gonzalez, 2013). Notably, *Drosophila* possesses a sole *PGC1* orthologue: *dPGC1*, also known as *spargel*, which has also been involved in the regulation of energy metabolism and mitochondrial function (Gershman *et al*, 2007; Mukherjee *et al*, 2014). The functional homology between dPGC1 and mammalian PGC1 members facilitates the study of PGC1 functions in *Drosophila* without the complications of redundancy.

The Hippo signaling pathway is a conserved regulator of normal and oncogenic growth. The central elements of this pathway comprise a regulatory kinase cascade that, when active, limits tissue growth by phosphorylating and inhibiting the activity of transcriptional coactivator with PDZ-binding motif

100 (TAZ) and Yes-associated protein (YAP), known as Yorkie (Yki) in *Drosophila* (Zheng & Pan,
101 2019). Deregulation of the activity of the Hippo pathway affects tumor development and has been
102 associated with traits of oncogenesis such as cell proliferation and survival, cancer metabolism,
103 invasion, and metastasis (Barron & Kagey, 2014; Moon *et al*, 2018). Consistent with their growth-
104 regulatory roles, YAP and TAZ are frequently amplified, while upstream elements in the pathway
105 are mutated in different cancer types (Calses *et al*, 2019).

106 Work from Banerjee's group (Nagaraj *et al*, 2012) demonstrated that activation of the Hippo pathway
107 effector Yki in *Drosophila* leads to increased mitochondrial fusion through the transcriptional
108 upregulation of key fusion genes such as *Mitofusin* (*dMfn* also known as *Marf*) and *Optic atrophy 1*
109 (*Opa1*). Their study showed that *Yki* overexpression alone is sufficient to induce mitochondrial
110 elongation and to upregulate several mitochondrial genes, including those involved in fusion and
111 oxidative stress responses, while notably not affecting *dPGC1* expression. These findings suggest
112 that Yki can directly modulate mitochondrial structure and function independently of dPGC1, and
113 that the regulation of mitochondrial fusion genes contributes to the growth-promoting role of Yki in
114 epithelial tissues. Building on this foundation, our study explores how *dPGC1* depletion further
115 modulates the transcriptional and morphological mitochondrial responses in a *Yki*-overexpressing
116 context. By comparing *Yki* overexpression alone to *Yki* upregulation combined with *dPGC1*
117 knockdown, we dissect the specific contributions of dPGC1 not only to mitochondrial dynamics and
118 gene regulation, but also to the tumor-like growth properties driven by Yki activation.

119 We find that while depletion of the transcriptional coactivator *dPGC1* has a minor impact on normal
120 *Drosophila* wing imaginal disc development, only causing a subtle growth defect, it dramatically
121 drives tumor growth and cellular transformation in imaginal discs overexpressing *Yki*. This
122 establishes dPGC1 as a context-dependent tumor suppressor that specifically limits Yki-driven tissue
123 overgrowth without altering *Yki* expression or activity, and notably, not affecting overgrowth by other
124 oncogenes. Tumors driven by *Yki* upregulation and *dPGC1* depletion exhibit enlarged mitochondria,
125 a phenotype that correlates with the transcriptional upregulation of key mitochondrial fusion genes,
126 *dMfn* and *Opa1*. We demonstrate that this is both necessary and sufficient to promote Yki-driven
127 oncogenic growth and malignancy. Tumors driven by *Yki* overexpression and *dPGC1* knockdown
128 show increased levels of Cyclin E protein. Cyclin E is essential for tumor development in this context,
129 promoting growth and inducing DNA damage, two hallmarks of cancer. This study elucidates a novel
130 connection between aberrant mitochondrial dynamics, defective cell cycle regulation, and DNA

damage in oncogenic processes occurring *in vivo*, suggesting that targeting mitochondrial fusion components may offer new therapeutic strategies to limit Yki/YAP-driven tumor growth.

133 # Results

134 ## dPGC1 is Required for Normal Wing Growth

135 The systemic functions of dPGC1 have been extensively studied, and it has been shown to control
136 central physiological processes such as early development, tissue homeostasis, obesity, and aging
137 (Chen *et al*, 2012; Diop *et al*, 2015; George & Jacobs, 2019; Mukherjee *et al.*, 2014; Mukherjee &
138 Duttaroy, 2013; Rera *et al*, 2011; Rogers & Rogina, 2014). However, its role in highly proliferative
139 tissues such as developing organs or neoplastic growth remains poorly understood. To address this
140 gap, we employed the *Drosophila* wing imaginal disc, a well-established *in vivo* model composed of
141 a proliferative epithelial monolayer that gives rise to the adult wing and thorax during metamorphosis.
142 This tissue serves as a powerful system for investigating epithelial development, growth regulation,
143 and tumorigenesis (Herranz *et al*, 2016).

144 To dissect the function of dPGC1 in this context, we examined the wings of $dPGC1^{1}$ mutant flies,
145 which carry a P-element insertion in the *dPGC1* gene. This insertion disrupts normal transcription
146 and results in reduced gene function (Tiefenbock *et al*, 2010). Despite this molecular alteration,
147 $dPGC1^{1}$ homozygous mutants are viable and do not display overt morphological abnormalities. These
148 observations are consistent with studies in mice showing that PGC1α and PGC1β are not essential
149 for normal development (Lelliott *et al*, 2006; Leone *et al*, 2005; Lin *et al.*, 2004; Sonoda *et al*, 2007;
150 Vianna *et al*, 2006). We detected a modest but statistically significant reduction in the size of both
151 wing discs and adult wings in $dPGC1^{1}/dPGC1^{1}$ mutants compared to controls (Fig 1A, B; Fig S1).
152 These results indicate that dPGC1, while not essential for viability or gross morphology, plays a role
153 in promoting normal wing growth. To confirm this role, we employed the Gal4-UAS binary system
154 to manipulate *dPGC1* expression in a spatially and temporally controlled manner (Brand & Perrimon,
155 1993). Using the MS1096-Gal4 driver, which is active in the wing disc epithelium (Fig 1C), we
156 specifically modulated gene activity during wing development and assessed the resulting adult
157 phenotypes. Consistent with the analysis of *dPGC1* mutants, expression of *dPGC1-RNAi* transgenes
158 under the control of MS1096-Gal4 led to a modest size reduction (Fig 1D, E). The efficiency of the
159 transgenes used to deplete *dPGC1* is shown in Fig S2. Overexpression of *dPGC1* did not affect wing
160 size or pattern (Fig 1D, E). These results indicate that, although dispensable for *Drosophila* viability,
161 dPGC1 is required for normal wing growth.

162 ## dPGC1 Restricts Yki-Driven Tissue Overgrowth in *Drosophila*

163 Given the role of dPGC1 in supporting normal wing growth, we next sought to determine whether
164 this transcriptional regulator also influences pathological growth conditions. Since many of the
165 molecular mechanisms that govern normal development are co-opted during tumorigenesis, we
166 hypothesized that dPGC1 might modulate the cellular response to oncogenic signals. Among the
167 various oncogenic drivers in *Drosophila*, we started analyzing the Hippo pathway effector Yki, a
168 conserved proto-oncogene that promotes tissue overgrowth and modulates mitochondrial structure
169 and function, processes in which dPGC1 is also implicated (Gerlach *et al*, 2018; Gerlach *et al*, 2019;
170 Huang *et al*, 2005; Nagaraj *et al.*, 2012; Nolo *et al*, 2006; Thompson & Cohen, 2006; Tiefenbock *et*
171 *al.*, 2010). This functional overlap in mitochondrial regulation provided a strong rationale to explore
172 whether dPGC1 modulates Yki-driven tumor-like growth. To test this, we depleted *dPGC1* in wing
173 imaginal discs overexpressing *Yki* using the apterous-Gal4 (ap-Gal4) driver, which has been
174 successfully employed to dissect various aspects of tumor formation (Eichenlaub *et al*, 2018; Gerlach
175 *et al.*, 2018; Herranz *et al*, 2012; Herranz *et al*, 2014; Song *et al*, 2019). As previously reported, *Yki*
176 overexpression leads to a marked increase in tissue size (Fig 2A, C, E) (Huang *et al.*, 2005). While
177 *dPGC1* knockdown alone did not affect wing disc size, its depletion in the context of *Yki*
178 overexpression significantly enhanced the overgrowth phenotype (Fig 2A–E). These findings indicate
179 that, although dPGC1 contributes modestly to normal wing development, it plays a critical role in
180 restraining Yki-driven tissue expansion.

181 To complement the overexpression studies and assess the role of dPGC1 in a more physiologically
182 relevant context, we analyzed *Warts* (*Wts*) mutant clones. Wts (Lats in mammals) is a core kinase in
183 the Hippo pathway that phosphorylates and inhibits Yki, preventing its nuclear localization. As
184 previously reported, loss of *Wts* mimics *Yki* overexpression and results in tissue overgrowth (Huang
185 *et al.*, 2005). Consistent with this, *Wts* mutant clones were larger than control clones (Fig 2F, G, I).
186 Notably, *Wts* mutant clones expressing *dPGC1-RNAi* exhibited even greater overgrowth (Fig 2G-I),
187 supporting the idea that dPGC1 acts to restrain tissue expansion in cells with elevated Yki activity.
188 These results validate our previous observations and further support a role for dPGC1 in limiting Yki-
189 driven tissue overgrowth.

190 To determine whether the enhanced growth phenotype observed upon *dPGC1* depletion could be
191 explained by increased *Yki* expression or activity, we used quantitative PCR (qPCR) to measure the
192 transcript levels of *Yki* and its target genes *Cyclin E*, *Diap1*, and *bantam* in wing imaginal discs with

193 or without *dPGC1* knockdown. These analyses revealed no significant changes, suggesting that the
194 phenotype is not driven by elevated *Yki* expression or transcriptional activity (Fig S3).

195 Given that dPGC1 modulates Yki-driven overgrowth, we asked whether it acts as a general regulator
196 of oncogenic growth or plays a more specific role in restraining Yki-induced tumorigenesis. To
197 address this, we downregulated *dPGC1* in tissues overexpressing the oncogenes *Epidermal Growth*
198 *Factor Receptor* (*EGFR*) or the *Insulin Receptor* (*InR*). In both cases, *dPGC1* depletion did not
199 enhance tissue overgrowth, in contrast to the effect observed in *Yki*-overexpressing discs (compare
200 Fig S4 with Fig 2C-E). This indicates that the tumor-suppressive role of dPGC1 is specifically
201 relevant in the context of Yki-driven tumorigenesis rather than being a general response to oncogenic
202 signaling.

203 **dPGC1 Restrains Oncogenic Traits in Yki-Induced Tumorous Discs**

204 Having established that dPGC1 limits Yki-driven tissue overgrowth, we next asked whether it also
205 suppresses other oncogenic traits associated with tumorigenesis. In addition to increased tissue size,
206 malignant fly tumors often express the secreted matrix metalloproteinase 1 (Mmp1), which promotes
207 cell migration and invasion by degrading the basement membrane (Beaucher *et al*, 2007; Uhlirova &
208 Bohmann, 2006). While we did not detect Mmp1 expression in control discs, Mmp1 was observed in
209 discrete patches of cells in discs overexpressing *Yki* (Fig 2J, K, M). Notably, discs co-expressing *Yki*
210 and *dPGC1-RNAi* displayed a robust increase in Mmp1 (Fig 2K-M). *Mmp1* is a target gene of the c-
211 Jun N-terminal kinase (JNK) pathway, a signaling cascade activated by internal and external stressors
212 that regulates proliferation, apoptosis, and cell migration (La Marca & Richardson, 2020; Pinal *et al*,
213 2019). JNK acts as an oncogenic partner of pro-tumorigenic factors such as Ras^{V12} and Yki (Igaki *et*
214 *al*, 2006; Uhlirova & Bohmann, 2006). In these contexts, JNK induces the accumulation of F-actin,
215 which is observed in cells undergoing malignant transformation (Enomoto *et al*, 2015; Fernandez *et*
216 *al*, 2011; Fernandez *et al*, 2014; George & Jacobs, 2019; Khoo *et al*, 2013; Uhlirova & Bohmann,
217 2006). Consistent with these findings, we observed elevated F-actin levels in *Yki* + *dPGC1-RNAi*
218 tumorous discs, along with increased expression of the JNK target gene *Mmp1* (Fig 2J-L, N). These
219 results were confirmed using an independent UAS-driven *dPGC1-shRNA* line (Fig S5), whose
220 knockdown efficiency is shown in Fig S2.

221 In addition to invasive and structural changes, uncontrolled proliferation is a hallmark of oncogenic
222 growth (Hanahan & Weinberg, 2011). To determine whether this feature was also present in *Yki* +

223 *dPGC1-RNAi* tumorous discs, we examined mitotic activity using phospho-Histone H3 (PH3)
224 staining, a well-established marker of cells undergoing mitosis and thus a proxy for cell proliferation.
225 This analysis revealed a significant increase in mitotic cells, indicating elevated proliferative activity
226 and highlighting an additional oncogenic feature of these tumors (Fig 2O-Q). These findings suggest
227 that *dPGC1* depletion not only enhances tissue overgrowth and promotes markers of malignancy but
228 also accelerates cell cycle progression in the context of Yki activation.

229 In sum, our results show that *dPGC1* knockdown enhances Yki-induced overgrowth, leading to the
230 formation of tumorous discs that exhibit markers of malignancy. Although *dPGC1* depletion does not
231 have a major impact on normal growth, it is required to maintain controlled growth and tissue integrity
232 in the context of *Yki* upregulation.

233 **Mitochondrial Membrane Potential in Yki-Driven Tumors**

234 Given the central role of dPGC1 in maintaining mitochondrial activity, we sought to evaluate
235 mitochondrial functionality in tumors driven by Yki activation and *dPGC1* depletion. As a surrogate
236 for mitochondrial function, we measured mitochondrial membrane potential (MMP). MMP is a key
237 indicator of mitochondrial function, reflecting the integrity of the electron transport chain and the
238 capacity for ATP production via oxidative phosphorylation. To evaluate MMP, we employed
239 tetramethylrhodamine ethyl ester (TMRE), a cell-permeant fluorescent dye that accumulates in
240 mitochondria in proportion to their electrochemical gradient (Ehrenberg *et al*, 1988). TMRE staining
241 showed no significant difference in MMP between discs expressing *Yki* alone and those co-expressing
242 *Yki* with *dPGC1-RNAi* (Fig S6). These results indicate that *dPGC1* depletion does not impair
243 mitochondrial membrane potential in Yki-driven tumors.

244 **dPGC1 Loss Selectively Upregulates Mitochondrial Fusion Genes in Yki-Driven Tumors**

245 Given that mitochondrial membrane potential was not significantly affected by *dPGC1* depletion in
246 Yki-driven tumors, we next investigated whether this genetic interaction alters the transcriptional
247 landscape of genes involved in mitochondrial dynamics. This analysis was motivated by previous
248 findings showing that PGC1 family proteins regulate the expression of genes involved in
249 mitochondrial biogenesis and function (Villena, 2015) and that Yki modulates mitochondrial
250 architecture to support tissue growth (Nagaraj *et al.*, 2012). We analyzed whether *dPGC1*
251 downregulation in the context of Yki activation affects the expression of genes involved in these

252 processes. By using qPCR, we compared the mRNA levels of genes involved in different aspects of
253 mitochondrial dynamics such as mitochondrial biogenesis, mitochondrial fusion and fission,
254 mitophagy, and mitochondrial transport (Archer, 2013). Among genes controlling mitochondrial
255 biogenesis, we quantified the expression of *estrogen-related receptor* (*dERR*), *Ets at 97D* (*Ets97D*),
256 and *erect wing* (*ewg*) (Baltzer et al, 2009; Chen et al, 2008; Misra et al, *2017*; Rai et al, 2014; Takata
257 et al, 2001). We also assessed the expression of the genes *dMfn* and *Opa1*, which control fusion
258 between outer and inner membranes, respectively; and *Dynamic-related protein 1* (*Drp1*), which
259 mediates mitochondrial fission (Deng et al, 2008). Additionally, we quantified the expression of
260 genes involved in mitophagy, including *PTEN-induced putative kinase 1* (*Pink1*), *parkin* (*park*), and
261 *Autophagy-related 7* (*Atg7*) (Narendra et al, 2010; Vincow et al, 2013). Finally, we measured the
262 levels of expression of genes involved in mitochondrial transport, such as *milton* (*milt*) and
263 *mitochondrial Rho* (*miro*) (Guo et al, 2005; Stowers et al, 2002). We analyzed four independent
264 biological replicates where we compared mRNA levels between *Yki*-upregulating discs (control) and
265 *Yki + dPGC1-RNAi* tumorous discs (experimental condition). We found that discs co-expressing *Yki*
266 and *dPGC1-RNAi* showed a significant increase in the expression of *dMfn* and *Opa1*, GTPases
267 promoting mitochondrial fusion (Fig 3A). Interestingly, *milt* and *miro* were also upregulated in *Yki +*
268 *dPGC1-RNAi* tumorous discs (Fig 3A). Although miro and milt play central roles in mitochondrial
269 axonal transport, previous reports have suggested that they can also affect mitochondrial morphology
270 (Ding *et al*, 2016; Liu & Hajnoczky, 2009; Panchal & Tiwari, 2020; Tang, 2015). For instance, *miro*
271 overexpression in *Drosophila* models of Alzheimer's disease has been reported to cause an increased
272 mitochondrial average length (Panchal & Tiwari, 2020).

273 *dPGC1* depletion in otherwise normal discs did not affect the expression of genes controlling
274 fusion/fission mechanisms to the same extent as observed in a context of *Yki* upregulation (Fig S7).
275 This observation suggests that the transcriptional response of mitochondrial dynamics genes to
276 *dPGC1* depletion is influenced by Yki activity, indicating that mitochondrial remodeling becomes
277 particularly responsive to *dPGC1* loss in an oncogenic environment driven by *Yki* upregulation.

278 To further explore the relationship between dPGC1 and mitochondrial fusion in the context of *Yki*
279 upregulation, we analyzed the expression of *dMfn* and *Opa1* in discs overexpressing *dPGC1*
280 alongside *Yki*. In contrast to the effects observed upon *dPGC1* downregulation, *dPGC1* upregulation
281 in *Yki*-overexpressing discs did not significantly affect tissue growth and did not alter *dMfn* and *Opa1*
282 mRNA levels (Fig S8). These findings suggest that the transcriptional upregulation of mitochondrial

283 fusion genes is a specific consequence of *dPGC1* knockdown in a Yki-activated context, highlighting
284 a sensitized mitochondrial response to Yki signaling rather than a general effect of altered dPGC1
285 levels.

286 **Functional Analysis of Mitochondrial Fusion Genes in Wing Disc Development**

287 The genes *dMfn, Opa1, milt,* and *miro*, which are upregulated in *Yki + dPGC1-RNAi* tumorous discs,
288 have been extensively studied in various model systems (Archer, 2013; Chan, 2020; Lee & Lu, 2014;
289 Zorzano *et al*, 2010). However, their specific functions in regulating mitochondrial morphology in
290 the *Drosophila* wing imaginal disc remain uncharacterized. To address this, we experimentally
291 manipulated the expression of these genes during wing disc development. To visualize mitochondria,
292 we used a mitochondrial-targeted GFP (Mito-GFP) transgene, which contains localization sequences
293 that direct GFP to the mitochondria (Rizzuto *et al*, 1995).

294 The wing imaginal disc is composed of two distinct epithelial layers: a densely packed columnar
295 epithelium, referred to as the main epithelium, and a squamous epithelium known as the peripodial
296 membrane (Gibson & Schubiger, 2001). The compact architecture and limited cytoplasmic volume
297 of the main epithelium pose challenges for high-resolution imaging of subcellular structures such as
298 mitochondria (Fig 3B). To circumvent these limitations, we performed mitochondrial imaging in the
299 peripodial membrane, which consists of large, flattened cells with expanded cytoplasmic space that
300 facilitates clear visualization of mitochondrial morphology. In this context, mitochondria appeared as
301 distinct and well-defined organelles (Fig 3C), enabling a reliable assessment of morphological
302 changes following genetic manipulations.

303 To assess the roles of genes upregulated in *Yki + dPGC1-RNAi* tumors, we used the Grunge-Gal4
304 (Gug-Gal4) driver to manipulate *dMfn, Opa1*, and *miro* specifically in the peripodial membrane of
305 the wing imaginal disc (Gibson *et al*, 2002). This allowed us to visualize mitochondrial changes
306 resulting from their experimental deregulation. dMfn and Opa1 are central regulators of
307 mitochondrial fusion. Upregulation of *dMfn* led to a connected mitochondrial network, indicative of
308 enhanced fusion (Fig 3D; quantified in Fig S9). In contrast, overexpression of *Opa1* produced a
309 subtler phenotype and mitochondria appeared slightly elongated compared to controls, but the overall
310 impact on network connectivity was modest relative to *dMfn* overexpression (compare Fig 3F with
311 Fig 3D; quantified in Fig S9). Depletion of *dMfn1* or *Opa1* led to mitochondrial fragmentation (Fig
312 3E, G; quantified in Fig S9). The phenotypic differences observed when *dMfn* and *Opa1* were

overexpressed likely reflect the distinct molecular roles of dMfn and Opa1 within the mitochondrial fusion machinery. While both proteins promote fusion, dMfn primarily facilitates the merging of the outer mitochondrial membrane, a process that directly contributes to the formation of interconnected networks. Opa1 regulates inner membrane fusion and cristae architecture, which may lead to elongation without extensive network formation.

milt and *miro* were also upregulated in *Yki + dPGC1-RNAi* tumors. Although milt and miro are traditionally associated with mitochondrial transport, recent studies suggest their involvement in mitochondrial dynamics (Ding *et al.*, 2016; Liu & Hajnoczky, 2009; Panchal & Tiwari, 2020; Tang, 2015). In our expression analysis, *miro* showed the highest level of upregulation between the two (Fig 3A), making it a particularly compelling candidate for functional investigation. Altering *miro* expression led to noticeable changes in mitochondrial morphology (Fig 3H, I; quantified in Fig S9). *miro* overexpression resulted in mitochondria that appeared elongated but not as extensively fused as those observed in *dMfn*-overexpressing imaginal discs (Fig 3H; quantified in Fig S9). The most pronounced effects were observed upon *miro* depletion. In these cells, mitochondria appeared smaller and more condensed, as indicated by the increased intensity and compaction of the Mito-GFP signal (Fig 3I; quantified in Fig S9). This phenotype differs qualitatively from the fragmentation seen with *dMfn* or *Opa1* knockdown and may reflect a different role in mitochondrial morphology. Given its established function in mitochondrial transport, *miro* downregulation may disrupt mitochondrial positioning and cytoskeletal interactions, leading to clustering rather than classical fragmentation.

The efficiency of the *UAS-RNAis* used to knock down *dMfn, Opa1*, and *miro* is shown in Fig S2.

Enhanced Mitochondrial Fusion in Yki-Driven Tumors Upon *dPGC1* Depletion

Our analyses have revealed transcriptional upregulation of mitochondrial fusion genes in *Yki + dPGC1-RNAi* tumors, suggesting a shift in mitochondrial dynamics. To investigate whether these transcriptional changes translate into altered mitochondrial morphology, we examined mitochondria in the tumorous tissue. Since the ap-Gal4 driver used to induce tumor formation is active in the main epithelium, which contains small, densely packed cells with limited cytoplasmic space, confocal imaging of mitochondria in this tissue proved technically challenging (Fig 3B). To overcome this limitation and obtain high-resolution structural information, we employed electron microscopy (EM) to assess mitochondrial morphology in Yki-driven tumors with or without *dPGC1* depletion.

342 Consistent with the upregulation of mitochondrial fusion genes such as *dMfn* and *Opa1*, we observed
343 that mitochondria in *Yki* + *dPGC1-RNAi* tumorous discs were larger and more elongated than those
344 in *Yki*-expressing discs (Fig 4A, B, D, E). Next, we assessed the consequences of downregulating
345 *dMfn*, the mitochondrial fusion gene showing the highest upregulation in *Yki* + *dPGC1-RNAi*
346 tumorous discs (Fig 3A). We found that mitochondria in tumors with reduced *dMfn* appeared larger
347 and more rounded compared to those in *Yki* + *dPGC1-RNAi* tumors (Fig 4B-E). Notably, these
348 swollen mitochondria exhibited disrupted cristae, with some displaying a characteristic onion-like
349 ultrastructure (Fig 4C, C'). In addition, we observed vesicle-like structures in those mitochondria,
350 further suggesting that cristae organization and mitochondrial integrity were compromised upon *dMfn*
351 depletion (Fig 4C, C'). These structural abnormalities suggest that cristae disorganization may impair
352 mitochondrial function, potentially disrupting energy production and cellular homeostasis, which
353 could in turn limit the ability of cells to sustain oncogenic growth.

354 **Contribution of Mitochondrial Fusion Genes to Yki-Mediated Tumor Growth**

355 Previous studies have shown that Yki upregulates genes involved in mitochondrial fusion, a process
356 that plays a central role in its growth-promoting activity (Nagaraj *et al.*, 2012). Building on this, we
357 demonstrate that depletion of *dPGC1* further enhances Yki-induced tissue overgrowth, with the
358 resulting tumorous discs exhibiting elongated mitochondria. These findings led us to hypothesize that
359 the upregulation of mitochondrial fusion genes may contribute to tumor formation when *Yki* is
360 overexpressed and *dPGC1* is knocked down. If this is the case, then reducing the expression of these
361 fusion-promoting genes should mitigate tumor growth. To test this, we used *UAS-RNAi* transgenes
362 targeting *dMfn* or *Opa1* in *Yki* + *dPGC1*-depleted tumors, which significantly reduced tissue growth
363 compared to control tumors (Fig 5A–D, G). These results indicate that mitochondrial fusion supports
364 tumor expansion in this context. Next, we investigated whether upregulation of mitochondrial fusion
365 genes alone is sufficient to drive tumorigenesis in cooperation with the proto-oncogene Yki. Co-
366 expression of *Yki* with either *dMfn* or *Opa1* led to a marked increase in disc size (Fig 5A, E–G),
367 indicating that enhanced mitochondrial fusion can potentiate Yki-driven tissue overgrowth.
368 Importantly, these tumors exhibited hallmark features of malignancy, including elevated expression
369 of *Mmp1* and disrupted epithelial architecture, as revealed by F-actin staining (Fig 5H, I). In contrast,
370 knockdown or overexpression of these fusion genes in otherwise normal discs resulted in only minor
371 changes in tissue size, effects that were significantly less pronounced than those observed in the tumor

372 context (Fig S10). Our findings highlight that dMfn and Opa1 are critical modulators of Yki-driven
373 tumorigenesis.

374 To further explore the oncogenic contribution of the genes upregulated in our expression analysis
375 (Fig 3A), we examined the function of miro. We found that, in contrast to *dMfn* and *Opa1*, *miro*
376 upregulation was not sufficient to drive tumorigenesis in combination with Yki. Moreover, *miro*
377 depletion did not alter the growth of *Yki* + *dPGC1-RNAi* tumors (Fig S11).

378 In summary, our results demonstrate that genes controlling mitochondrial morphology play a gene-
379 specific and context-dependent role in Yki-mediated tumorigenesis. While upregulation of fusion
380 genes such as *dMfn* and *Opa1* synergizes with *Yki* to promote tissue overgrowth and malignancy,
381 *miro* does not exhibit the same oncogenic potential.

382 **Upregulation of Cyclin E in Tumors Caused by *Yki* upregulation and *dPGC1* Depletion**

383 Mounting evidence has established a connection between mitochondrial dynamics and the cell cycle
384 (Ma *et al*, 2020). Proper control of the cell cycle is essential for accurate genome transmission during
385 cell division, and its disruption can lead to genomic instability, which is a hallmark of cancer.
386 (Hanahan, 2022; Hanahan & Weinberg, 2011). Cyclin-dependent kinases (CDKs) and their
387 regulatory cyclins are well-established drivers of cell cycle progression (Besson *et al*, 2008;
388 Satyanarayana & Kaldis, 2009). Beyond these canonical regulators, mitochondria have emerged as
389 key modulators of cell cycle control, with their dynamic behavior contributing to the maintenance of
390 genomic stability (Horbay & Bilyy, 2016; Lopez-Mejia & Fajas, 2015; Mandal *et al*, 2005; Owusu-
391 Ansah *et al*, 2008).

392 Studies in mammalian cells and in *Drosophila* have shown that cells with highly fused mitochondria
393 present an elevation in the levels of the oncogene *Cyclin E* (Finkel & Hwang, 2009; Mitra, 2013;
394 Mitra *et al*, 2012; Mitra *et al*, 2009; Qian *et al.*, 2012). Cyclin E peaks at the G1-S transition,
395 activating CDK2 and promoting S phase entry (Siu *et al*, 2012). Aberrant Cyclin E levels can trigger
396 premature entry in S phase, leading to replicative stress and DNA damage, which are key contributors
397 to genomic instability in cancer (Gaillard *et al*, 2015; Molano-Fernandez *et al*, 2022; Saxena & Zou,
398 2022).

399 We have shown that *dPGC1* depletion in epithelial cells with elevated Yki signaling leads to an
400 increase in mitochondrial size, which correlates with the transcriptional upregulation of genes

401 promoting mitochondrial fusion, and is associated with tumor formation. These observations
402 prompted us to investigate whether *Yki* + *dPGC1-RNAi* tumors exhibit abnormal levels of Cyclin E.
403 We first examined *cyclin E* mRNA levels and found no significant differences between discs
404 expressing *Yki* alone and those co-expressing *Yki* with *dPGC1-RNAi* (Fig 6A). Interestingly, although
405 transcript levels remained unchanged, Cyclin E protein levels were elevated in tumors driven by *Yki*
406 overexpression and *dPGC1* depletion (Fig 6B, C; Fig S12). These results indicate that Cyclin E
407 upregulation occurs post-transcriptionally and are consistent with previous studies linking
408 mitochondria to Cyclin E regulation through non-transcriptional mechanisms (Mandal *et al.*, 2005;
409 Owusu-Ansah *et al.*, 2008).

410 Aberrant Cyclin E levels can lead to replicative stress and DNA damage in human cells and
411 *Drosophila* (Ekholm-Reed *et al*, 2004; Molano-Fernandez *et al.*, 2022; Spruck *et al*, 1999). In
412 response to DNA damage, checkpoint proteins phosphorylate the histone H2AX (H2Av in
413 *Drosophila*) to mark the sites of damage (Blackford & Jackson, 2017; Fernandez-Capetillo *et al*,
414 2003). Antibodies recognizing the phosphorylated H2Av (pH2Av) can serve as markers to detect
415 DNA damage. As expected, *Yki* overexpression led to an increase in pH2Av-positive foci (Fig 6D, E,
416 H). Notably, this effect was enhanced when *dPGC1* was knocked down (Fic 6E, F, H), which is
417 consistent with an increase in Cyclin E. These observations revealed that *dPGC1* depletion in discs
418 activating the *Yki* proto-oncogene leads to an increase in Cyclin E levels and DNA damage.

419 Oncogene-induced DNA damage is a mutagenic source in cancer, and DNA damage can promote
420 tumorigenesis in *Drosophila* (Dekanty *et al*, 2015; Gerlach & Herranz, 2020; Halazonetis *et al*, 2008).
421 We then analyzed whether Cyclin E upregulation contributes to the growth of *Yki* + *dPGC1-RNAi*
422 tumors. To investigate the role of Cyclin E dosage in tumor growth, we induced the formation *Yki* +
423 *dPGC1-RNAi* tumors in a *Cyclin E* heterozygous (+/-) background and analyzed whether reduced
424 Cyclin E levels affected tumor development. We observed that *Cyclin E* heterozygous discs did not
425 display any growth defects (Fig 6I, J, O). However, when *Yki* was overexpressed and *dPGC1* was
426 depleted in a *Cyclin E* heterozygous background, tumor size was dramatically reduced, indicating
427 that reduced *Cyclin E* dosage specifically impairs tumor growth under these conditions (Fig 6M, N,
428 O). This suggests that Cyclin E upregulation is a central factor driving tumorigenesis in *Yki* + *dPGC1-*
429 *RNAi* tumors.

430 Next, we asked whether upregulation of Cyclin E was sufficient to enhance Yki-driven growth.
431 Cyclin E activity is negatively regulated by the Cyclin E-dependent kinase inhibitor p21/dacapo

432 (dap), which represses Cyclin E/CDK2 function. Therefore, reduced levels of dap increase Cyclin
433 E/CDK2 activity (de Nooij *et al*, 1996; Lane *et al*, 1996). To test this, we depleted *dap* in *Yki*-
434 expressing discs and found that this was sufficient to significantly enhance tumor growth (Fig 6K, L,
435 O), supporting the idea that elevated Cyclin E activity promotes Yki-driven tumorigenesis.
436 Interestingly, similar to what we observed in the *Yki* + *dPGC1-RNAi* context, *Yki* + *dap-RNAi* tumors
437 also exhibited increased levels of DNA damage (Fig 6E, G, H), suggesting that Cyclin E upregulation
438 may contribute to genomic instability in these tumors. The efficiency of *UAS-dap-RNAi* is shown in
439 Fig S13. In sum, these results reveal that *dPGC1* downregulation in the context of Yki activation
440 leads to Cyclin E upregulation, which promotes the accumulation of DNA damage and drives
441 increased tumor growth.

442 Finaly, to determine whether the increase in Cyclin E is a general consequence of *dPGC1* depletion
443 or specific to the oncogenic context of Yki activation, we analyzed Cyclin E levels in $dPGC1^{1}$
444 homozygous mutant wing discs (-/-) in the absence of *Yki* overexpression. We did not observe any
445 detectable changes in Cyclin E protein levels under these conditions (Fig S14). This indicates that
446 *dPGC1* depletion alone is not sufficient to stabilize Cyclin E and further supports the notion that the
447 oncogenic traits observed, such as Cyclin E accumulation, are specific to the context of *Yki*
448 upregulation.

449 **Discussion**

450 Our findings demonstrate that dPGC1 functions as a tumor suppressor by limiting Yki-driven tissue
451 overgrowth in the *Drosophila* wing imaginal disc. Under normal conditions, *dPGC1* mutants exhibit
452 only a minor growth defect, and altering dPGC1 levels during physiological wing development does
453 not lead to overt phenotypes. This indicates that dPGC1 is largely dispensable for normal tissue
454 growth but becomes critical under oncogenic stress, particularly when Yki is hyperactivated. These
455 observations align with recent work by the Halder group, which shows that Yki/YAP transcriptional
456 input is not required for normal growth but instead drives ectopic tissue expansion through the
457 induction of an aberrant genetic program (Kowalczyk *et al*, 2022). Such aberrant activation represents
458 a pathological stress condition, further supporting the idea that dPGC1 is required to maintain tissue
459 integrity under oncogenic challenges.

460 This selective requirement becomes even more striking when considering its specificity. Although
461 dPGC1 does not modulate tumor-like growth driven by other oncogenic signals such as EGFR or
462 InR, it plays a crucial role in suppressing Yki-induced overgrowth. Importantly, this suppression
463 occurs without altering Yki expression or activity, suggesting that dPGC1 acts downstream or in
464 parallel to Yki signaling. In this context, dPGC1 influences the transcription of mitochondrial fusion
465 genes, pointing to a role in modulating mitochondrial dynamics in response to Yki-driven oncogenic
466 stress. This is consistent with previous findings that link changes in mitochondrial morphology to the
467 growth-promoting effects of Yki (Nagaraj *et al.*, 2012), reinforcing a model in which dPGC1
468 safeguards tissue integrity by regulating mitochondrial function under pathological conditions.

469 This context-dependent role is consistent with observations in mammalian systems. For example,
470 PGC1α knockout mice develop normally, indicating that PGC1 family members are not required for
471 normal development (Leone *et al.*, 2005), However, under stress conditions, PGC1α mutant mice
472 exhibit a range of physiological defects, highlighting the importance of PGC1α in maintaining
473 cellular homeostasis during pathological challenges (Arany *et al*, 2005; Lin *et al.*, 2004). A similar
474 context-specific function has been described for PGC1α in oncogenic processes. Its expression is
475 frequently downregulated in various tumor types, suggesting a tumor-suppressive role (Feilchenfeldt
476 *et al*, 2004; Torrano *et al.*, 2016; Watkins *et al*, 2004; Zhang *et al*, 2007). Conversely, other studies
477 have shown that PGC1α can promote tumorigenesis and metastasis in certain cellular and tissue
478 contexts (Bhalla *et al.*, 2011; LeBleu *et al*, 2014). Together, these findings highlight the importance

479 of the cellular context in determining the pro- or antitumorigenic roles of these transcriptional
480 regulators.

481 Yki promotes tissue overgrowth by regulating gene expression through its interaction with the TEAD
482 transcription factor Scalloped, inducing targets such as *Cyclin E* and mitochondrial fusion genes like
483 *dMfn* and *Opa1* (Bandura & Edgar, 2008; Nagaraj *et al.*, 2012; Shu & Deng, 2017; Tapon *et al*, 2002).
484 Our data show that *dPGC1* depletion in the context of Yki hyperactivation leads to upregulation of
485 mitochondrial fusion genes, enlarged mitochondria, and enhanced tumor growth. These observations
486 align with previous studies showing that increased mitochondrial fusion supports proliferation in Ras-
487 transformed fibroblasts and *Drosophila* stem cells (Dubal *et al*, 2022; Garcez *et al*, 2020; Yao *et al*,
488 2019). Importantly, this regulation appears to be context-dependent, as *dPGC1* depletion in otherwise
489 normal discs has little or no detectable impact on the expression of mitochondrial fusion and fission
490 genes. These findings suggest that dPGC1 dampens the ability of Yki to induce the expression of
491 genes inducing mitochondrial fusion, thereby limiting oncogenic proliferation. Supporting this,
492 reducing dMfn levels in *Yki + dPGC1-RNAi* discs disrupt mitochondrial morphology and impairs
493 tumor growth. EM analyses of these discs reveal swollen mitochondria with disorganized cristae,
494 structures essential for respiration and ATP production. Such defects likely compromise
495 mitochondrial function and contribute to reduced tumor expansion. Beyond their roles in fusion, Opa1
496 and Mfn2 also regulate cristae architecture and mitochondrial-ER contacts, which are critical for
497 apoptosis, oxidative phosphorylation, and calcium signaling (Frezza *et al*, 2006; Naon *et al*, 2023).
498 While our results support a role for enhanced mitochondrial fusion in Yki-driven tumorigenesis, we
499 acknowledge that mitochondrial enlargement may also result from reduced fission activity or
500 imbalances in mitochondrial biogenesis and mitophagy. Future studies employing live-cell imaging
501 and dynamic assays will be essential to fully characterize the mitochondrial remodeling events
502 underlying oncogenic transformation in this context. These broader functions may help explain how
503 altered mitochondrial structure and inter-organelle communication contribute to the oncogenic
504 phenotype.

505 Alterations in mitochondrial structure and function can influence key cell cycle regulators, linking
506 metabolic and structural changes to proliferative outcomes (Lopez-Mejia & Fajas, 2015; Mandal *et*
507 *al.*, 2005; Mitra, 2013; Mitra *et al.*, 2009; Owusu-Ansah *et al.*, 2008). Mitochondrial fusion has been
508 shown to stabilize and increase Cyclin E levels, promoting G1–S progression (Finkel & Hwang, 2009;
509 Mitra, 2013). Consistent with this, our results show that *dPGC1* depletion in the context of *Yki*

510 upregulation leads to increased Cyclin E protein levels. This correlates with elevated DNA damage,
511 a hallmark of genomic instability commonly observed in tumors (Tubbs & Nussenzweig, 2017). We
512 provide experimental evidence that Cyclin E upregulation is essential for tumor growth in this setting,
513 identifying it as a central oncogenic driver in *Yki + dPGC1* knockdown tumors.

514 In sum, our findings demonstrate that *dPGC1* deregulation in cells with Yki activation leads to
515 aberrant mitochondrial dynamics, increased Cyclin E levels, and DNA damage, factors that converge
516 on key hallmarks of cancer, including altered cell proliferation, metabolism, and genomic instability.
517 These results underscore the complexity of mitochondrial regulation in tumor biology and highlight
518 the need to dissect the specific contributions of individual regulators of mitochondrial function.
519 Targeting components of the mitochondrial fusion machinery may offer novel therapeutic strategies
520 to limit Yki/YAP-driven tumor growth.

521 ## Materials and Methods

522 ***Drosophila* strains**

523 The following stocks used in this paper were obtained from the Bloomington *Drosophila* Stock
524 Center: *dPGC1*^{1} (synonym of *srl*^{KG08646}) (14965), *hsFLP, UAS-GFP.U;; tub-Gal4 FRT82B, tub-*
525 *Gal80* (86311), *FRT82B* (2051), *FRT82B Wts*^{X1} (44251), *Gug-Gal4* (6773), *act-Gal4* (4414), *Mito-*
526 *GFP* (8443), *yw* (1495), *UAS-LacZ* (3956), *UAS-dPGC1*^{RNAi} (33914), *EP-dPGC1* (20009), *UAS-*
527 *dMfn* (67157), *UAS-dMfn*^{RNAi} (55189), *EP-Opa1* (20054), *UAS-Opa1*^{RNAi} (32358), *UAS-miro*
528 (51646), and *UAS-dap*^{RNAi} (64026). The *UAS-dPGC1*^{shRNA} (v330271) and *miro*^{RNAi} (v106683) stocks
529 were obtained from the Vienna *Drosophila* Stock Center. The *CycE*^{05306} stock was a kind gift from
530 Helena Richardson. The following stocks used in this study are described in the following references:
531 *MS1096-Gal4* (Capdevila & Guerrero, 1994), *ap-Gal4 (Calleja et al, 1996)*, *UAS-Yki (Huang et al.,*
532 *2005)*, *UAS-InR29.4* (*UAS-InR*) (Mirth *et al*, 2005), and *UAS-EGFR* (Buff *et al*, 1998).
533 *Drosophila* strains were raised on food that was made in-house containing agar (8g/L), brewer's yeast
534 (23.6g/L), dextrose (50.8g/L) and corn meal (58g/L). Depending on the experiment, flies were housed
535 in humidity-controlled incubators set at either 18°C or 25°C with a 12/12-hour light dark cycle.

536 **List of Genotypes**

537 Figure 1
538 (A, B) *yw* corresponds to *yw/yw.*
539 *dPGC1*^{1} *corresponds to dPGC1*^{1}*/dPGC1*^{1}.
540 (C-E) Control corresponds to *MS1096-Gal4, UAS-RFP/+; +/+; UAS-LacZ/+.*
541 *MS1096>dPGC1*^{RNAi} corresponds to *MS1096-Gal4, UAS-RFP/+; +/+; UAS-dPGC1*^{RNAi}*/+.*
542 *MS1096>dPGC1* corresponds to *MS1096-Gal4, UAS-RFP/+; +/+; EP-dPGC1/+.*

543 Figure 2
544 (A-E; J-Q) Control corresponds to *ap-Gal4, UAS-CD8-GFP/+; tub-Gal80ts/UAS-LacZ.*
545 *ap>dPGC1*^{RNAi} corresponds to *ap-Gal4, UAS-CD8-GFP/+; tub-Gal80ts/UAS-dPGC1*^{RNAi}.
546 *ap>Yki* corresponds to *ap-Gal4, UAS-CD8-GFP/+; UAS-Yki, tub-Gal80ts/UAS-LacZ.*
547 *ap>Yki+dPGC1*^{RNAi} corresponds to *ap-Gal4, UAS-CD8-GFP/+; UAS-Yki, tub-Gal80ts/UAS-*
548 *dPGC1*^{RNAi}.
549 (F-I) Control corresponds to *hsFLP, UAS-GFP.U/+; +/+; tub-GAL4 FRT82B tub-*
550 *GAL80/FRT82B Sb.*

551 *Wts^{X1}* corresponds to *hsFLP, UAS-GFP.U/+; +/+; tub-Gal4 FRT82B tub-Gal80/FRT82B Wts^{X1}*.
552 *Wts^{X1}+dPGC1^{shRNA}* corresponds to *hsFLP, UAS-GFP.U/+; UAS-dPGC1^{shRNA}/+; tub-Gal4*
553 *FRT82B tub-Gal80/ FRT82B Wts^{X1}*.

554 Figure 3
555 (A) The experimental condition corresponds to *ap-Gal4, UAS-CD8-GFP/+; UAS-Yki, tub-*
556 *Gal80ts/UAS-dPGC1^{RNAi}* and the control used for normalization corresponds to *ap-Gal4, UAS-*
557 *CD8-GFP/+; UAS-Yki, tub-Gal80ts/UAS-LacZ.*
558 (B) *ap-Gal4/+; UAS-Mito-GFP/+*.
559 (C) *Gug-Gal4, UAS-Mito-GFP/+*.
560 (D) *Gug-Gal4, UAS-Mito-GFP/UAS-dMfn.*
561 (E) *UAS-dMfn^{RNAi}/+; Gug-Gal4, UAS-Mito-GFP/+*.
562 (F) *EP-Opa1/+; Gug-Gal4, UAS-Mito-GFP/+*.
563 (G) *Gug-Gal4, UAS-Mito-GFP/UAS-Opa1^{RNAi}*.
564 (H) *UAS-miro/+; Gug-Gal4, UAS-Mito-GFP/+*.
565 (I) *UAS-miro^{RNAi}/+; Gug-Gal4, UAS-Mito-GFP/+*.

566 Figure 4
567 *ap>Yki* corresponds to *ap-Gal4, UAS-CD8-GFP/+; UAS-Yki, tub-Gal80ts/UAS-LacZ.*
568 *ap>Yki+dPGC1^{RNAi}* corresponds to *ap-Gal4, UAS-CD8-GFP/+; UAS-Yki, tub-Gal80ts/UAS-*
569 *dPGC1^{RNAi}*.
570 *ap>Yki+dPGC1^{RNAi}+dMfn^{RNAi}* corresponds to *ap-Gal4, UAS-CD8-GFP/UAS-dMfn^{RNAi}; UAS-*
571 *Yki, tub-Gal80ts/UAS-dPGC1^{RNAi}*.

572 Figure 5
573 Control corresponds to *ap-Gal4, UAS-CD8-GFP/+; tub-Gal80ts/UAS-LacZ.*
574 *ap>Yki* corresponds to *ap-Gal4, UAS-CD8-GFP/+; UAS-Yki, tub-Gal80ts/UAS-LacZ.*
575 *ap>Yki+dPGC1^{RNAi}* corresponds to *ap-Gal4, UAS-CD8-GFP/+; UAS-Yki, tub-Gal80ts/UAS-*
576 *dPGC1^{RNAi}*.
577 *ap>Yki+dPGC1^{RNAi}+dMfn^{RNAi}* corresponds to *ap-Gal4, UAS-CD8-GFP/UAS-dMfn^{RNAi}; UAS-*
578 *Yki, tub-Gal80ts/UAS-dPGC1^{RNAi}*.
579 *ap>Yki+dPGC1^{shRNA}* corresponds to *ap-Gal4, UAS-CD8-GFP/UAS-dPGC1^{shRNA}; UAS-Yki, tub-*
580 *Gal80ts/+*.

581 *ap>Yki+dPGC1^{shRNA}+Opa1^{RNAi}* corresponds to *ap-Gal4, UAS-CD8-GFP/UAS-dPGC1^{shRNA};*
582 *UAS-Yki, tub-Gal80ts/UAS-Opa1^{RNAi}*.
583 *ap>Yki+dMfn* corresponds to *ap-Gal4, UAS-CD8-GFP/+; UAS-Yki, tub-Gal80ts/UAS-dMfn.*
584 *ap>Yki+Opa1* corresponds to *ap-Gal4, UAS-CD8-GFP/EP-Opa1; UAS-Yki, tub-Gal80ts/+.*

585 Figure 6
586 Control corresponds to *ap-Gal4, UAS-CD8-GFP/+; tub-Gal80ts/UAS-LacZ.*
587 *ap>; CycE^{05306}* corresponds to *ap-Gal4, UAS-CD8-GFP/CycE^{05306}; tub-Gal80ts/+.*
588 *ap>Yki* corresponds to *ap-Gal4, UAS-CD8-GFP/+; UAS-Yki, tub-Gal80ts/UAS-LacZ.*
589 *ap>Yki+dap^{RNAi}* corresponds to *ap-Gal4, UAS-CD8-GFP/UAS-dap^{RNAi}; UAS-Yki, tub-Gal80ts/+.*
590 *ap>Yki+dPGC1^{RNAi}* corresponds to *ap-Gal4, UAS-CD8-GFP/+; UAS-Yki, tub-Gal80ts/UAS-*
591 *dPGC1^{RNAi}*.
592 *ap>Yki+dPGC1^{RNAi}; CycE^{05306}* corresponds to *ap-Gal4, UAS-CD8-GFP/CycE^{05306}; UAS-Yki,*
593 *tub-Gal80ts/UAS-dPGC1^{RNAi}*.

594 Figure S1
595 *yw* corresponds to *yw/yw.*
596 *dPGC1^{1} corresponds to dPGC1^{1}/dPGC1^{1}*.

597 Figure S2
598 *act>* corresponds to *act-Gal4/+.*
599 *act>dPGC1^{RNAi}* corresponds to *act-Gal4/UAS-dPGC1^{RNAi}*.
600 *act>dPGC1^{shRNA}* corresponds to *dPGC1^{shRNA}/+; act-Gal4/+.*
601 *act>dMfn* corresponds to *act-Gal4/UAS-dMfn.*
602 *act>dMfn^{RNAi}* corresponds to *UAS-dMfn^{RNAi}/+; act-Gal4/+.*
603 *act>Opa1* corresponds to *EP-Opa1/+; act-Gal4/+.*
604 *act>Opa1^{RNAi}* corresponds to *act-Gal4/UAS-Opa1^{RNAi}*.
605 *act>miro* corresponds to *UAS-miro/+; act-Gal4/+.*
606 *act>miro^{RNAi}* corresponds to *UAS-miro^{RNAi}/+; act-Gal4/+.*

607 Figure S3
608 Control corresponds to *ap-Gal4, UAS-CD8-GFP/+; tub-Gal80ts/UAS-LacZ.*
609 *ap>dPGC1^{RNAi}* corresponds to *ap-Gal4, UAS-CD8-GFP/+; tub-Gal80ts/UAS-dPGC1^{RNAi}*.

610 Figure S4

611 (A-C) *ap>EGFR* corresponds to *ap-Gal4, UAS-CD8-GFP/+; UAS-EGFR, tub-Gal80ts/+.*

612 *ap>EGFR+dPGC1*^{RNAi} corresponds to *ap-Gal4, UAS-CD8-GFP/+; UAS-EGFR, tub-*

613 *Gal80ts/UAS-dPGC1*^{RNAi}.

614 (D-F) *ap>InR* corresponds to *ap-Gal4, tub-Gal80ts/+; UAS-InR/+.*

615 *ap>InR+dPGC1*^{RNAi} corresponds to *ap-Gal4, tub-Gal80ts/+; UAS-InR/UAS-dPGC1*^{RNAi}.

616 Figure S5

617 Control corresponds to *ap-Gal4, UAS-CD8-GFP/+; tub-Gal80ts/UAS-LacZ.*

618 *ap>dPGC1*^{shRNA} corresponds to *ap-Gal4, UAS-CD8-GFP/ UAS-dPGC1*^{shRNA}*; tub-Gal80ts/+.*

619 *ap>Yki* corresponds to *ap-Gal4, UAS-CD8-GFP/+; UAS-Yki, tub-Gal80ts/UAS-LacZ.*

620 *ap>Yki+dPGC1*^{shRNA} corresponds to *ap-Gal4, UAS-CD8-GFP/UAS-dPGC1*^{shRNA}*; UAS-Yki, tub-*

621 *Gal80ts/+.*

622 Fig S6

623 *ap>Yki* corresponds to *ap-Gal4, UAS-CD8-GFP/+; UAS-Yki, tub-Gal80ts/UAS-LacZ.*

624 *ap>Yki+dPGC1*^{RNAi} corresponds to *ap-Gal4, UAS-CD8-GFP/+; UAS-Yki, tub-Gal80ts/UAS-*

625 *dPGC1*^{RNAi}.

626 Fig S7

627 The experimental condition corresponds to *ap-Gal4, UAS-CD8-GFP/+; tub-Gal80ts/UAS-*

628 *dPGC1*^{RNAi} and the control used for normalization corresponds to *ap-Gal4, UAS-CD8-GFP/+;*

629 *tub-Gal80ts/UAS-LacZ.*

630 Fig S8

631 *ap>Yki* corresponds to *ap-Gal4, UAS-CD8-GFP/+; UAS-Yki, tub-Gal80ts/UAS-LacZ.*

632 *ap>Yki+dPGC1* corresponds to *ap-Gal4, UAS-CD8-GFP/+; UAS-Yki, tub-Gal80ts/EP-dPGC1.*

633 Figure S9

634 Control corresponds to *Gug-Gal4, UAS-Mito-GFP/+.*

635 *Gug>dMfn* corresponds to *Gug-Gal4, UAS-Mito-GFP/UAS-dMfn.*

636 *Gug>Mfn*^{RNAi} corresponds to *UAS-dMfn*^{RNAi}*/+; Gug-Gal4, UAS-Mito-GFP/+.*

637 *Gug>Opa1* corresponds to *EP-Opa1/+; Gug-Gal4, UAS-Mito-GFP/+.*

638 *Gug>Opa1*^{RNAi} corresponds to *Gug-Gal4, UAS-Mito-GFP/UAS-Opa1*^{RNAi}.

639 *Gug>miro* corresponds to *UAS-miro/+; Gug-Gal4, UAS-Mito-GFP/+*.

640 *Gug>miro^{RNAi}* corresponds to *UAS-miro^{RNAi}/+; Gug-Gal4, UAS-Mito-GFP/+*.

641 Figure S10

642 Control corresponds to *ap-Gal4, UAS-CD8-GFP/+; tub-Gal80ts/UAS-LacZ.*

643 *ap>Mfn* corresponds to *ap-Gal4, UAS-CD8-GFP/+; tub-Gal80ts/ UAS-dMfn.*

644 *ap>Mfn^{RNAi}* corresponds to *ap-Gal4, UAS-CD8-GFP/ UAS-dMfn^{RNAi}; tub-Gal80ts/+*.

645 *ap>Opa1* corresponds to *ap-Gal4, UAS-CD8-GFP/EP-Opa1; tub-Gal80ts/+*.

646 *ap>Opa1^{RNAi}* corresponds to *ap-Gal4, UAS-CD8-GFP/+; tub-Gal80ts/ UAS-Opa1^{RNAi}*.

647 Figure S11

648 (A-C) *ap>Yki+dP*GC1^{RNAi} corresponds to *ap-Gal4, UAS-CD8-GFP/+; UAS-Yki, tub-*
649 *Gal80ts/UAS-dP*GC1^{RNAi}.

650 *ap>Yki+dP*GC1^{RNAi}*+miro^{RNAi}* corresponds to *ap-Gal4, UAS-CD8-GFP/UAS-miro^{RNAi}; UAS-Yki,*
651 *tub-Gal80ts/UAS-dP*GC1^{RNAi}.

652 (D-F) *ap>Yki* corresponds to *ap-Gal4, UAS-CD8-GFP/+; UAS-Yki, tub-Gal80ts/UAS-LacZ.*

653 *ap>Yki+miro* corresponds to *ap-Gal4, UAS-CD8-GFP/UAS-miro; UAS-Yki, tub-Gal80ts/+*.

654 Figure S12

655 *ap>Yki* corresponds to *ap-Gal4, UAS-CD8-GFP/+; UAS-Yki, tub-Gal80ts/UAS-LacZ.*

656 *ap>Yki+dPGC1^{RNAi}* corresponds to *ap-Gal4, UAS-CD8-GFP/+; UAS-Yki, tub-Gal80ts/UAS-*
657 *dPGC1^{RNAi}*.

658 Figure S13

659 *ap>Yki* corresponds to *ap-Gal4, UAS-CD8-GFP/+; UAS-Yki, tub-Gal80ts/UAS-LacZ.*

660 *ap>Yki+dap^{RNAi}* corresponds to *ap-Gal4, UAS-CD8-GFP/UAS-dap^{RNAi}; UAS-Yki, tub-Gal80ts/+*.

661 Figure S14

662 *yw* corresponds to *yw/yw.*

663 *dPGC1^{1} corresponds to dPGC1^{1}/dPGC1^{1}*.

664 **Temporal Control of Transgene Expression by Gal80^{ts}**

665 For experiments using ap-Gal4 or act-Gal4, the Gal4/Gal80^{ts} system was used to prevent lethality
666 during early development. This system allowed UAS-driven transgenes to be controlled in a
667 temperature-dependent manner. *Drosophila* crosses were kept for 2 days at 18°C to lay eggs. After 2

668 days, crosses were flipped into new vials and the old vials containing eggs were kept for 2 additional
669 days at 18°C before being transferred to a 29°C incubator for transgene expression to be induced. To
670 ensure that wing discs were analyzed at the same developmental stage, larvae with hyperplastic
671 tumors were dissected after 5 days at 29°C, whereas giant larvae containing neoplastic tumors were
672 dissected after 7 days at 29°C.

673 **Induction of Mitotic Clones**

674 Mitotic recombination clones were generated using the FLP/FRT system, employing the MARCM
675 (Mosaic Analysis with a Repressible Cell Marker) technique. Larvae carrying the necessary
676 transgenes (see the list of genotypes for details) were maintained at 25°C for 48–96 hours after egg
677 laying. To induce FLP recombinase expression, vials were heat-shocked by immersion in a
678 circulating water bath at 37°C for 60 minutes. Following heat shock, larvae were returned to 25°C
679 and allowed to develop for an additional 96 hours to permit clone growth. Larvae were dissected at
680 the third instar wandering stage, corresponding to 96 hours after heat shock, for analysis of imaginal
681 discs.

682 **Immunohistochemistry**

683 Larvae were dissected in PBS and fixed in 3.7% formaldehyde / PBS for 20 minutes at room
684 temperature. Samples were then washed in 0.2% Triton / PBS (PBT) and blocked for an hour at room
685 temperature in blocking buffer (BBT) made of 0.2% Triton, 5mM NaCl, and 3% BSA diluted in PBS.
686 Primary antibodies were diluted in BBT, and the samples were left in primary antibody solution
687 overnight at room temperature. Longer primary antibody incubations were done at 4°C. After
688 removing the primary antibody and performing washes with BBT, samples were incubated for 2 hours
689 at room temperature with the relevant fluorescent secondary antibodies and DAPI diluted in BBT.
690 After removing the secondary antibody and performing washes with PBT, samples were mounted in
691 90% glycerol / PBS containing 0.5% N-propyl gallate. Samples were imaged with the Leica SP8
692 confocal microscope. For stainings intended for mitochondrial analysis, BBT and PBT contained
693 0.2% Tween instead of 0.2% Triton.
694 The following primary antibodies were used: mouse anti-MMP1 (Developmental Studies Hybridoma
695 Bank, 3A6B4/5H7B11/3B8D12 mixed in equal volumes), rabbit anti-pH2Av (Rockland, 600-401-
696 914, dilution 1:1000), rabbit anti-PH3 (Cell Signal Technology, 9701, dilution 1:100), and rabbit anti-
697 Cyclin E (Santa Cruz, 33748, dilution 1:100). The following secondary antibodies were used: Alexa
698 Fluor 635-phalloidin to stain F-actin (Invitrogen, A34054, dilution 1:200), anti-mouse Alexa Fluor

699 555 (Invitrogen, A21425, dilution 1:200), and anti-rabbit Alexa Fluor 555 (Invitrogen, A21430,
700 dilution 1:200). DAPI (Invitrogen, D1306) was used at a 600 nM concentration to stain the nuclei.

701 **Analysis of Mitochondrial Membrane Potential**

702 Wing discs from *Drosophila* larvae were dissected in Schneider's medium (Sigma, Ref: S9895). After
703 dissection, wing discs were incubated in 100 nM TMRE (Sigma, Ref: 87917, dissolved in Schneider's
704 medium) for 20 minutes with agitation. Then, wing discs were washed once with Schneider's medium
705 for 5 minutes, rinsed with PBS, and mounted in Schneider's medium. Samples were immediately
706 imaged after mounting with the Leica SP8 confocal microscope. All steps were performed at room
707 temperature.

708 **Electron Microscopy**

709 Larval wing discs were dissected in PBS and fixed in 2% glutaraldehyde / 0.1M sodium cacodylate
710 buffer at room temperature. Sample preparation was performed by the Core Facility for Integrative
711 Microscopy at the University of Copenhagen, where tissues were fixed, embedded, stained,
712 dehydrated, infiltrated, embedded, and cut into thin sections for imaging. All specimens were imaged
713 at the Core Facility for Integrative Microscopy with a Transmission Electron Microscope (Philips
714 CM100, FEL). Digital images were recorded with an OSIS Veleta digital slow-scan 2k x 2k CCD
715 camera and the ITEM software package. Mitochondrial morphologies reflected in these 2D
716 micrographs were analyzed with Fiji software. Mitochondria were manually outlined and quantified
717 for area, perimeter, and aspect ratio (calculated as MaxFeret/MinFeret to assess elongation). At least
718 164 mitochondria were quantified per genotype.

719 **RNA Extraction, cDNA Synthesis, and qPCR**

720 For experiments performed with ap-Gal4, RNA was extracted from wing discs dissected from third
721 instar wandering larvae with the TRIzol reagent (Life Technologies, Ref: 15596026). For experiments
722 performed with act-Gal4, RNA was extracted from whole third instar wandering larvae with the
723 RNeasy Mini Kit (Qiagen, Ref: 74106). Total RNA was treated with RQ1 DNase I (Promega, Ref:
724 M6101) and converted to cDNA using the SuperScript III Reverse Transcriptase kit (Life
725 technologies, Ref: 18080-044). qPCR was performed using 5x HOT FIREPol EvaGreen qPCR Mix
726 Plus (Solis Biodyne, Ref: 08-24-00001) on the QuantStudio 6 Flex Real-Time PCR machine (Applied
727 Biosystems). The primers used are listed below.

Gene	**Forward primer sequence:**	**Reverse primer sequence:**
dPGC1	GCTGACTTGGATAATGCTGGCA	TGAACCTACCGGTGACTTGC

dERR	GGAATTGGTCAGCGTCATTGG	GAACTCCGTGTAACCGCACT
Ets97D	GGTGCCCTGGAAGAAGTGATT	ACGCATTGGTCCACGAGATT
ewg	CGATGTTGATTACACCACGCA	TTTGAATGGTAGCACCGCCT
dMfn	AGCAGTATTGGACACAGCGT	ACGCCAGCCGATAGTTTTCA
Opa1	CCCATGAAGGCTTTGGGCTA	ACCCCTCGACGATGGAAAAG
Drp1	AGATGCTGCGCTTTCCCAAA	AGTAGGGATCGCTGTCCGTT
Pink1	TACCGACAGGACCAATTGCC	CCACTGTAGGATCTCCGGACT
Park	CGGATGTGAGTGATACCGTGT	TACTCCTCGCGTGTCAACAG
Atg7	GTGACACGACCCGGAGTATC	ATTTAGGACGGCCGCTGAAC
milt	AAGGACCTAGAGCTGACCGT	GGAGTGTCAGTATCTGTGCCA
miro	TATTCCACCATGGACAGCGT	CGGATGTGAGCTCCTGTTCTTC
CycE	TTCTACCAGCAGCACTGAGC	TGGAAGGATAGCGATTGGGC
Yki	GATCTGGCCATCATTGGTCT	GTCATCAGCCCCATTCAGTT
Diap1	ATGAGAGTGATGTCTGCTGCTCTTC	AGCTGATGAAGGGTCAGCTCTATATC
Ban	ACCGGTTTTCGATTTGGTTT	ACCATCGGAATGTGGAATGT
Dap	TGGCAATGCGGCTTAGCTC	GCTTTGCGGGCGATAGTTTCT
RP49	AAGCGGCGACGCACTCTGTT	GCCCAGCATACAGGCCCAAG

Western Blot

Wing discs were dissected from *Drosophila* larvae and transferred into RIPA protein extraction and immunoprecipitation buffer (Sigma-Aldrich, Ref: R0278) containing cOmplete Protease Inhibitor Cocktail (Merck, Ref: 04693124001), PhosSTOP (Merck, Ref: 04906837001), and 100mM PMSF (Sigma-Aldrich, Ref: 93482). Wing discs were homogenized by pipetting up and down and then leaving samples on ice for 30 minutes. Afterwards, samples were sonicated three times for three cycles with the following settings: 100% amplitude, 1 cycle. Samples were then centrifuged for 20 minutes at 15000g and 4°C to obtain the supernatant that was used for western blots. Protein concentration was quantified using the Pierce BCA protein assay kit (Thermo Fisher Scientific, Ref: 23227). Western blots were performed using 15 µg of protein per sample. Western blot membranes were blocked for an hour at room temperature with 5% skimmed milk (Fluka, Ref: 70166-500G) dissolved in TBST. After washing with TBST, the membranes were incubated overnight at 4°C with primary antibodies diluted in TBST. After removing the primary antibody and performing washes with TBST, samples were incubated for 1 hour at room temperature with the relevant HRP-conjugated secondary antibodies. After removing the secondary antibodies and washing with TBST, the Pierce ECL Western Blotting Substrate kit (Thermo Fisher Scientific, Ref: 32106) was used to visualize protein levels on the Amersham Imager 600 (GE Healthcare).

The following primary antibodies were used: rabbit anti-Cyclin E (Santa Cruz, 33748, dilution 1:1000) and mouse anti-α-Tubulin (Developmental Studies Hybridoma Bank, 12G10, dilution 1:1000). The following HRP-conjugated secondary antibodies were used: polyclonal goat anti-rabbit-

748 HRP (Invitrogen, 31460, dilution 1:10000) and polyclonal goat anti-mouse-HRP (Dako, P0447,
749 dilution 1:5000). Note that since Cyclin E and α-Tubulin have similar molecular weights, membranes
750 had to be stripped to detect both proteins without any crossover.

751 **Image Analysis and Processing**

752 Image analyses were performed using Fiji (ImageJ) software. Specific quantification procedures are
753 described in the sections below. Final figures were assembled using Adobe Photoshop.

754 **Quantification of *Drosophila* Wing Imaginal Disc and Clone Size**

755 To quantify wing imaginal disc size, the "threshold" function was first used to select either the GFP-
756 positive area or the DAPI-positive area, depending on the experiment. After setting a threshold, areas
757 were determined using the "analyze particles" option. A minimum of 10 discs were quantified per
758 genotype. To quantify clone size, individual clones in each wing disc were selected with the
759 "polygon" tool, and their area was directly measured using the "measure" option. For each genotype,
760 at least 65 clones were quantified from a total of a minimum of 10 discs. For both wing disc and clone
761 size quantifications, results were expressed as the fold change of GFP or DAPI area relative to the
762 corresponding control.

763 **Quantification of *Drosophila* Adult Wing Size**

764 Crosses were allowed to lay eggs on apple agar plates with yeast paste at 25°C for 10 to 14 hours.
765 Once eggs hatched and L1 larvae emerged, 20 larvae were transferred to vials containing standard
766 *Drosophila* food, and these vials were kept at 25°C until adult flies eclosed. Wings were fixed by
767 introducing adult flies into a 25% glycerol / 75% ethanol mixture for at least 24 hours. After that,
768 wings were plucked and mounted in glycerol for imaging. Images of adult *Drosophila* wings were
769 taken with a Leica M165 stereomicroscope.
770 To measure adult wing area, the "polygon" selection tool in Fiji was used to draw a border around
771 the wing edges. Next, the "measure" option was used to quantify the wing area. Results were
772 expressed as the fold change in wing area relative to the control. A total of 20 wings were quantified
773 per genotype.

774 **Quantification of Mitochondrial Shape in the Peripodial Membrane**

775 The Gug-Gal4 driver was used to drive the expression of the *Mito-GFP* mitochondria marker in the
776 peripodial membrane. After obtaining images of peripodial membrane cells, two filters were applied
777 to the GFP channel, unsharp mask (radius = 10.0 pixels, mask strength = 0.9) and median filtering

778 (radius = 3), to enhance and smooth the Mito-GFP signal, respectively (Terriente-Felix *et al*, 2020).
779 Next, the "threshold" function was used to create a binary mask, and the "Mitochondrial Analyzer
780 2D Analysis" plugin from ImageJ (Chaudhry *et al*, 2020) was used to calculate the mean form factor.
781 Mitochondria from a minimum of 15 images were quantified per genotype.

782 **Quantification of TMRE Intensity**

783 For each image, the area of the wing disc containing mitochondria stained with TMRE was selected
784 using the "threshold" function on the TMRE channel. The mean gray value of only the thresholded
785 selection was obtained with the "measure" function. Results were expressed as the fold change of
786 TMRE intensity relative to the control. Importantly, comparisons were only made between wing discs
787 that had been stained and imaged together, meaning that fold changes were always calculated
788 considering the mean of the control for each individual experiment and then all fold changes were
789 pooled for the statistical analysis. For each genotype, a minimum of 23 wing discs from a total of 5
790 experiments were quantified.

791 **Quantification of Mmp1 Area**

792 For each wing disc, the GFP-positive area was first measured as explained above and the GFP
793 selection was added to the ROI manager. Afterwards, a "gaussian blur" filter of 1 was applied to the
794 Mmp1 channel and the "threshold" function was used to select only the Mmp1-positive signal. The
795 thresholded Mmp1 area within the previously selected GFP area was measured with the "measure"
796 option within the ROI manager. Results were expressed as the Mmp1 area normalized to the GFP-
797 positive area. A minimum of 11 wing discs were quantified per genotype.

798 **Quantification of F-actin and Cyclin E Intensity**

799 Quantification of F-actin and Cyclin E intensities were done with the same procedure. The "polygon"
800 tool was first used to select a DAPI-positive and GFP-positive (if applicable) area within the image.
801 Then, the mean gray value of the corresponding channel (either F-actin or Cyclin E) within the
802 selected area was obtained with the "measure" function. Results were expressed as the direct values
803 of mean intensity (for F-actin) or as the fold change in mean intensity relative to the control (for
804 Cyclin E). A minimum of 19 wing discs (for F-actin) or 13 wing discs (for Cyclin E) were quantified
805 per genotype.

806 **Quantification of PH3-Positive Cells**

807 First, the “polygon” tool was used to select a DAPI-positive and GFP-positive area, which was then
808 measured with the “measure” function. Then, a “gaussian blur” filter of 3 was applied to the PH3
809 channel. Finally, the number of PH3-positive cells was measured with the “find maxima” tool.
810 Results were expressed as the number of PH3-positive cells per GFP-positive area. A minimum of
811 19 wing discs were quantified per genotype.

812 **Quantification of pH2Av-Positive Foci**

813 Maximum projections of Z-stack images of wing discs were used for this quantification. First, the
814 GFP-positive area was measured as previously described. Then, the number of pH2Av-positive foci
815 was measured using the “3D Objects Counter”. Results were expressed as the fold change in number
816 of pH2Av-positive foci per area relative to the control. A minimum of 18 wing discs were quantified
817 per genotype.

818 **Quantification of Protein Levels in Western Blot Membranes**

819 Western blot membranes were loaded to Fiji, and the “rectangle” tool was used to select the
820 corresponding bands, fitting all genotypes in the same rectangle. Within the “gels” function, “select
821 first lane” was used to set this rectangle as a lane, and then “plot lanes” was used to generate a lane
822 profile plot showcasing intensity peaks corresponding to each band within the rectangle. The “line”
823 tool was used to draw base lines for each peak, generating closed areas that did not include the
824 background signal, and these peak areas were then measured. For each genotype, areas obtained for
825 Cyclin E bands were normalized to the corresponding α-Tubulin bands. Results were expressed as
826 the fold change in Cyclin E/α-Tubulin peak areas for each membrane, and then all fold changes were
827 pooled for the statistical analysis. A total of 7 western blot membranes were quantified.

828 **Statistics**

829 Graphs and statistical analyses were done using GraphPad Prism 10. Data is always presented as full-
830 range box plots. The number of biological replicates quantified per sample and the statistical tests
831 applied to determine statistical significance are indicated in the corresponding figure legends.

Acknowledgements

We thank Helena Richardson, Kim F. Rewitz, and Takashi Koyama for reagents. We thank Bloomington *Drosophila* Stock Center and Vienna *Drosophila* Resource Center for fly stocks; Developmental Studies Hybridoma Bank for antibodies; and the fly community for sharing reagents. We also thank the Center for Integrated Microscopy (CFIM) at the University of Copenhagen for electron microscopy support.

Conflict of interest

The authors declare that the research was conducted in the absence of any commercial or financial relationships that could be construed as a potential conflict of interest.

Funding

This work was supported by the Independent Research Fund Denmark Grant 0134-00045B, Novo Nordisk Foundation Grant NNF18OC0052223, a grant from the Neye Foundation, and a grant from Grosserer Alfred Nielsen og Hustru's fond.

845 ## References

846 Abu Shelbayeh O, Arroum T, Morris S, Busch KB (2023) PGC-1alpha Is a Master Regulator of
847 Mitochondrial Lifecycle and ROS Stress Response. *Antioxidants (Basel)* 12

848 Adebayo M, Singh S, Singh AP, Dasgupta S (2021) Mitochondrial fusion and fission: The fine-tune
849 balance for cellular homeostasis. *FASEB J* 35: e21620

850 Antico Arciuch VG, Elguero ME, Poderoso JJ, Carreras MC (2012) Mitochondrial regulation of cell
851 cycle and proliferation. *Antioxid Redox Signal* 16: 1150-1180

852 Arany Z, He H, Lin J, Hoyer K, Handschin C, Toka O, Ahmad F, Matsui T, Chin S, Wu PH *et al* (2005)
853 Transcriptional coactivator PGC-1 alpha controls the energy state and contractile function of cardiac
854 muscle. *Cell Metab* 1: 259-271

855 Archer SL (2013) Mitochondrial dynamics--mitochondrial fission and fusion in human diseases. *N*
856 *Engl J Med* 369: 2236-2251

857 Baltzer C, Tiefenbock SK, Marti M, Frei C (2009) Nutrition controls mitochondrial biogenesis in the
858 Drosophila adipose tissue through Delg and cyclin D/Cdk4. *PLoS One* 4: e6935

859 Bandura JL, Edgar BA (2008) Yorkie and Scalloped: partners in growth activation. *Dev Cell* 14: 315-
860 316

861 Barron DA, Kagey JD (2014) The role of the Hippo pathway in human disease and tumorigenesis. *Clin*
862 *Transl Med* 3: 25

863 Beaucher M, Hersperger E, Page-McCaw A, Shearn A (2007) Metastatic ability of Drosophila tumors
864 depends on MMP activity. *Dev Biol* 303: 625-634

865 Besson A, Dowdy SF, Roberts JM (2008) CDK inhibitors: cell cycle regulators and beyond. *Dev Cell*
866 14: 159-169

867 Bhalla K, Hwang BJ, Dewi RE, Ou L, Twaddel W, Fang HB, Vafai SB, Vazquez F, Puigserver P, Boros L
868 *et al* (2011) PGC1alpha promotes tumor growth by inducing gene expression programs supporting
869 lipogenesis. *Cancer Res* 71: 6888-6898

870 Blackford AN, Jackson SP (2017) ATM, ATR, and DNA-PK: The Trinity at the Heart of the DNA Damage
871 Response. *Mol Cell* 66: 801-817

872 Brand AH, Perrimon N (1993) Targeted gene expression as a means of altering cell fates and
873 generating dominant phenotypes. *Development* 118: 401-415

874 Buff E, Carmena A, Gisselbrecht S, Jimenez F, Michelson AM (1998) Signalling by the Drosophila
875 epidermal growth factor receptor is required for the specification and diversification of embryonic
876 muscle progenitors. *Development* 125: 2075-2086

877 Calleja M, Moreno E, Pelaz S, Morata G (1996) Visualization of gene expression in living adult
878 Drosophila. *Science* 274: 252-255

879 Calses PC, Crawford JJ, Lill JR, Dey A (2019) Hippo Pathway in Cancer: Aberrant Regulation and
880 Therapeutic Opportunities. *Trends Cancer* 5: 297-307

881 Capdevila J, Guerrero I (1994) Targeted expression of the signaling molecule decapentaplegic
882 induces pattern duplications and growth alterations in Drosophila wings. *The EMBO journal* 13:
883 4459-4468

884 Chan DC (2020) Mitochondrial Dynamics and Its Involvement in Disease. *Annu Rev Pathol* 15: 235-
885 259

886 Chaudhry A, Shi R, Luciani DS (2020) A pipeline for multidimensional confocal analysis of
887 mitochondrial morphology, function, and dynamics in pancreatic beta-cells. *Am J Physiol Endocrinol*
888 *Metab* 318: E87-E101

889 Chen J, Shi X, Padmanabhan R, Wang Q, Wu Z, Stevenson SC, Hild M, Garza D, Li H (2008)
890 Identification of novel modulators of mitochondrial function by a genome-wide RNAi screen in
891 Drosophila melanogaster. *Genome Res* 18: 123-136

892 Chen L, Qin Y, Liu B, Gao M, Li A, Li X, Gong G (2022) PGC-1alpha-Mediated Mitochondrial Quality
893 Control: Molecular Mechanisms and Implications for Heart Failure. *Front Cell Dev Biol* 10: 871357

894 Chen S, Oliveira MT, Sanz A, Kemppainen E, Fukuoh A, Schlicht B, Kaguni LS, Jacobs HT (2012) A
895 cytoplasmic suppressor of a nuclear mutation affecting mitochondrial functions in Drosophila.
896 *Genetics* 192: 483-493

897 Dai W, Jiang L (2019) Dysregulated Mitochondrial Dynamics and Metabolism in Obesity, Diabetes,
898 and Cancer. *Front Endocrinol (Lausanne)* 10: 570

899 de Nooij JC, Letendre MA, Hariharan IK (1996) A cyclin-dependent kinase inhibitor, Dacapo, is
900 necessary for timely exit from the cell cycle during Drosophila embryogenesis. *Cell* 87: 1237-1247

901 Dekanty A, Barrio L, Milan M (2015) Contributions of DNA repair, cell cycle checkpoints and cell
902 death to suppressing the DNA damage-induced tumorigenic behavior of Drosophila epithelial cells.
903 *Oncogene* 34: 978-985

904 Deng H, Dodson MW, Huang H, Guo M (2008) The Parkinson's disease genes pink1 and parkin
905 promote mitochondrial fission and/or inhibit fusion in Drosophila. *Proc Natl Acad Sci U S A* 105:
906 14503-14508

907 Ding L, Lei Y, Han Y, Li Y, Ji X, Liu L (2016) Vimar Is a Novel Regulator of Mitochondrial Fission through
908 Miro. *PLoS Genet* 12: e1006359

909 Diop SB, Bisharat-Kernizan J, Birse RT, Oldham S, Ocorr K, Bodmer R (2015) PGC-1/Spargel
910 Counteracts High-Fat-Diet-Induced Obesity and Cardiac Lipotoxicity Downstream of TOR and
911 Brummer ATGL Lipase. *Cell Rep* 10: 1572-1584

912 Dubal D, Moghe P, Verma RK, Uttekar B, Rikhy R (2022) Mitochondrial fusion regulates proliferation
913 and differentiation in the type II neuroblast lineage in Drosophila. *PLoS Genet* 18: e1010055

914 Ehrenberg B, Montana V, Wei MD, Wuskell JP, Loew LM (1988) Membrane potential can be
915 determined in individual cells from the nernstian distribution of cationic dyes. *Biophys J* 53: 785-794

916 Eichenlaub T, Villadsen R, Freitas FCP, Andrejeva D, Aldana BI, Nguyen HT, Petersen OW, Gorodkin
917 J, Herranz H, Cohen SM (2018) Warburg Effect Metabolism Drives Neoplasia in a Drosophila Genetic
918 Model of Epithelial Cancer. *Curr Biol* 28: 3220-3228 e3226

919 Ekholm-Reed S, Mendez J, Tedesco D, Zetterberg A, Stillman B, Reed SI (2004) Deregulation of cyclin
920 E in human cells interferes with prereplication complex assembly. *J Cell Biol* 165: 789-800

921 Enomoto M, Kizawa D, Ohsawa S, Igaki T (2015) JNK signaling is converted from anti- to pro-tumor
922 pathway by Ras-mediated switch of Warts activity. *Dev Biol* 403: 162-171

923 Feilchenfeldt J, Brundler MA, Soravia C, Totsch M, Meier CA (2004) Peroxisome proliferator-
924 activated receptors (PPARs) and associated transcription factors in colon cancer: reduced
925 expression of PPARgamma-coactivator 1 (PGC-1). *Cancer Lett* 203: 25-33

926 Fernandez-Capetillo O, Celeste A, Nussenzweig A (2003) Focusing on foci: H2AX and the recruitment
927 of DNA-damage response factors. *Cell Cycle* 2: 426-427

928 Fernandez BG, Gaspar P, Bras-Pereira C, Jezowska B, Rebelo SR, Janody F (2011) Actin-Capping
929 Protein and the Hippo pathway regulate F-actin and tissue growth in Drosophila. *Development* 138:
930 2337-2346

931 Fernandez BG, Jezowska B, Janody F (2014) Drosophila actin-Capping Protein limits JNK activation
932 by the Src proto-oncogene. *Oncogene* 33: 2027-2039

933 Finkel T, Hwang PM (2009) The Krebs cycle meets the cell cycle: mitochondria and the G1-S
934 transition. *Proc Natl Acad Sci U S A* 106: 11825-11826

935 Frezza C, Cipolat S, Martins de Brito O, Micaroni M, Beznoussenko GV, Rudka T, Bartoli D, Polishuck
936 RS, Danial NN, De Strooper B *et al* (2006) OPA1 controls apoptotic cristae remodeling independently
937 from mitochondrial fusion. *Cell* 126: 177-189

938 Gaillard H, Garcia-Muse T, Aguilera A (2015) Replication stress and cancer. *Nat Rev Cancer* 15: 276-
939 289

940 Garcez M, Branco-Santos J, Gracio PC, Homem CCF (2020) Mitochondrial Dynamics in the Drosophila
941 Ovary Regulates Germ Stem Cell Number, Cell Fate, and Female Fertility. *Front Cell Dev Biol* 8:
942 596819

943 George J, Jacobs HT (2019) Germline knockdown of spargel (PGC-1) produces embryonic lethality in
944 Drosophila. *Mitochondrion* 49: 189-199

945 Gerlach SU, Eichenlaub T, Herranz H (2018) Yorkie and JNK Control Tumorigenesis in Drosophila Cells
946 with Cytokinesis Failure. *Cell Rep* 23: 1491-1503

947 Gerlach SU, Herranz H (2020) Genomic instability and cancer: lessons from Drosophila. *Open Biol*
948 10: 200060

949 Gerlach SU, Sander M, Song S, Herranz H (2019) The miRNA bantam regulates growth and
950 tumorigenesis by repressing the cell cycle regulator tribbles. *Life Sci Alliance* 2

951 Gershman B, Puig O, Hang L, Peitzsch RM, Tatar M, Garofalo RS (2007) High-resolution dynamics of
952 the transcriptional response to nutrition in Drosophila: a key role for dFOXO. *Physiol Genomics* 29:
953 24-34

954 Gibson MC, Lehman DA, Schubiger G (2002) Lumenal transmission of decapentaplegic in Drosophila
955 imaginal discs. *Dev Cell* 3: 451-460

956 Gibson MC, Schubiger G (2001) Drosophila peripodial cells, more than meets the eye? *Bioessays* 23:
957 691-697

958 Girnun GD (2012) The diverse role of the PPARγ coactivator 1 family of transcriptional coactivators
959 in cancer. *Seminars in cell & developmental biology* 23: 381-388

960 Gonzalez C (2013) Drosophila melanogaster: a model and a tool to investigate malignancy and
961 identify new therapeutics. *Nat Rev Cancer* 13: 172-183

962 Guo X, Macleod GT, Wellington A, Hu F, Panchumarthi S, Schoenfield M, Marin L, Charlton MP,
963 Atwood HL, Zinsmaier KE (2005) The GTPase dMiro is required for axonal transport of mitochondria
964 to Drosophila synapses. *Neuron* 47: 379-393

965 Halazonetis TD, Gorgoulis VG, Bartek J (2008) An oncogene-induced DNA damage model for cancer
966 development. *Science* 319: 1352-1355

967 Hanahan D (2022) Hallmarks of Cancer: New Dimensions. *Cancer Discov* 12: 31-46

968 Hanahan D, Weinberg RA (2011) Hallmarks of cancer: the next generation. *Cell* 144: 646-674

969 Herranz H, Eichenlaub T, Cohen SM (2016) Cancer in Drosophila: Imaginal Discs as a Model for
970 Epithelial Tumor Formation. *Curr Top Dev Biol* 116: 181-199

971 Herranz H, Hong X, Hung NT, Voorhoeve PM, Cohen SM (2012) Oncogenic cooperation between
972 SOCS family proteins and EGFR identified using a Drosophila epithelial transformation model. *Genes*
973 *Dev* 26: 1602-1611

974 Herranz H, Weng R, Cohen SM (2014) Crosstalk between epithelial and mesenchymal tissues in
975 tumorigenesis and imaginal disc development. *Curr Biol* 24: 1476-1484

976 Horbay R, Bilyy R (2016) Mitochondrial dynamics during cell cycling. *Apoptosis* 21: 1327-1335

977 Huang J, Wu S, Barrera J, Matthews K, Pan D (2005) The Hippo signaling pathway coordinately
978 regulates cell proliferation and apoptosis by inactivating Yorkie, the Drosophila Homolog of YAP.
979 *Cell* 122: 421-434

980 Igaki T, Pagliarini RA, Xu T (2006) Loss of cell polarity drives tumor growth and invasion through JNK
981 activation in Drosophila. *Curr Biol* 16: 1139-1146

982 Jones AW, Yao Z, Vicencio JM, Karkucinska-Wieckowska A, Szabadkai G (2012) PGC-1 family
983 coactivators and cell fate: roles in cancer, neurodegeneration, cardiovascular disease and
984 retrograde mitochondria-nucleus signalling. *Mitochondrion* 12: 86-99

985 Khoo P, Allan K, Willoughby L, Brumby AM, Richardson HE (2013) In Drosophila, RhoGEF2 cooperates
986 with activated Ras in tumorigenesis through a pathway involving Rho1-Rok-Myosin-II and JNK
987 signalling. *Dis Model Mech* 6: 661-678

988 Kowalczyk W, Romanelli L, Atkins M, Hillen H, Bravo Gonzalez-Blas C, Jacobs J, Xie J, Soheily S,
989 Verboven E, Moya IM *et al* (2022) Hippo signaling instructs ectopic but not normal organ growth.
990 *Science* 378: eabg3679

991 La Marca JE, Richardson HE (2020) Two-Faced: Roles of JNK Signalling During Tumourigenesis in the
992 Drosophila Model. *Front Cell Dev Biol* 8: 42

993 Lane ME, Sauer K, Wallace K, Jan YN, Lehner CF, Vaessin H (1996) Dacapo, a cyclin-dependent kinase
994 inhibitor, stops cell proliferation during Drosophila development. *Cell* 87: 1225-1235

995 LeBleu VS, O'Connell JT, Gonzalez Herrera KN, Wikman H, Pantel K, Haigis MC, de Carvalho FM,
996 Damascena A, Domingos Chinen LT, Rocha RM *et al* (2014) PGC-1alpha mediates mitochondrial
997 biogenesis and oxidative phosphorylation in cancer cells to promote metastasis. *Nat Cell Biol* 16:
998 992-1003, 1001-1015

999 Lee KS, Lu B (2014) The myriad roles of Miro in the nervous system: axonal transport of mitochondria
1000 and beyond. *Front Cell Neurosci* 8: 330

1001 Lelliott CJ, Medina-Gomez G, Petrovic N, Kis A, Feldmann HM, Bjursell M, Parker N, Curtis K,
1002 Campbell M, Hu P *et al* (2006) Ablation of PGC-1beta results in defective mitochondrial activity,
1003 thermogenesis, hepatic function, and cardiac performance. *PLoS Biol* 4: e369

1004 Leone TC, Lehman JJ, Finck BN, Schaeffer PJ, Wende AR, Boudina S, Courtois M, Wozniak DF,
1005 Sambandam N, Bernal-Mizrachi C *et al* (2005) PGC-1alpha deficiency causes multi-system energy
1006 metabolic derangements: muscle dysfunction, abnormal weight control and hepatic steatosis. *PLoS*
1007 *Biol* 3: e101

1008 Liao JZ, Chung HL, Shih C, Wong KKL, Dutta D, Nil Z, Burns CG, Kanca O, Park YJ, Zuo Z *et al* (2024)
1009 Cdk8/CDK19 promotes mitochondrial fission through Drp1 phosphorylation and can phenotypically
1010 suppress pink1 deficiency in Drosophila. *Nat Commun* 15: 3326

1011 Liesa M, Borda-d'Agua B, Medina-Gomez G, Lelliott CJ, Paz JC, Rojo M, Palacin M, Vidal-Puig A,
1012 Zorzano A (2008) Mitochondrial fusion is increased by the nuclear coactivator PGC-1beta. *PLoS One*
1013 3: e3613

1014 Lin J, Wu H, Tarr PT, Zhang CY, Wu Z, Boss O, Michael LF, Puigserver P, Isotani E, Olson EN *et al* (2002)
1015 Transcriptional co-activator PGC-1 alpha drives the formation of slow-twitch muscle fibres. *Nature*
1016 418: 797-801

1017 Lin J, Wu PH, Tarr PT, Lindenberg KS, St-Pierre J, Zhang CY, Mootha VK, Jager S, Vianna CR, Reznick
1018 RM *et al* (2004) Defects in adaptive energy metabolism with CNS-linked hyperactivity in PGC-1alpha
1019 null mice. *Cell* 119: 121-135

1020 Liu X, Hajnoczky G (2009) Ca2+-dependent regulation of mitochondrial dynamics by the Miro-Milton
1021 complex. *Int J Biochem Cell Biol* 41: 1972-1976

1022 Lopez-Mejia IC, Fajas L (2015) Cell cycle regulation of mitochondrial function. *Curr Opin Cell Biol* 33:
1023 19-25

1024 Ma Y, Wang L, Jia R (2020) The role of mitochondrial dynamics in human cancers. *Am J Cancer Res*
1025 10: 1278-1293

1026 Mandal S, Guptan P, Owusu-Ansah E, Banerjee U (2005) Mitochondrial regulation of cell cycle
1027 progression during development as revealed by the tenured mutation in Drosophila. *Dev Cell* 9: 843-
1028 854

1029 Mirth C, Truman JW, Riddiford LM (2005) The role of the prothoracic gland in determining critical
1030 weight for metamorphosis in Drosophila melanogaster. *Curr Biol* 15: 1796-1807

1031 Mishra P, Chan DC (2014) Mitochondrial dynamics and inheritance during cell division, development
1032 and disease. *Nat Rev Mol Cell Biol* 15: 634-646

1033 Misra S, Pandey AK, Gupta S, Kumar A, Khanna P, Shankar J, Ravi Ram K (2017) Estrogen related
1034 receptor is required for the testicular development and for the normal sperm
1035 axoneme/mitochondrial derivatives in Drosophila males. *Sci Rep* 7: 40372

1036 Mitra K (2013) Mitochondrial fission-fusion as an emerging key regulator of cell proliferation and
1037 differentiation. *Bioessays* 35: 955-964

1038 Mitra K, Rikhy R, Lilly M, Lippincott-Schwartz J (2012) DRP1-dependent mitochondrial fission
1039 initiates follicle cell differentiation during Drosophila oogenesis. *J Cell Biol* 197: 487-497

1040 Mitra K, Wunder C, Roysam B, Lin G, Lippincott-Schwartz J (2009) A hyperfused mitochondrial state
1041 achieved at G1-S regulates cyclin E buildup and entry into S phase. *Proc Natl Acad Sci U S A* 106:
1042 11960-11965

1043 Molano-Fernandez M, Hickson ID, Herranz H (2022) Cyclin E overexpression in the Drosophila
1044 accessory gland induces tissue dysplasia. *Front Cell Dev Biol* 10: 992253

1045 Moon S, Yeon Park S, Woo Park H (2018) Regulation of the Hippo pathway in cancer biology. *Cell*
1046 *Mol Life Sci* 75: 2303-2319

1047 Mukherjee S, Basar MA, Davis C, Duttaroy A (2014) Emerging functional similarities and divergences
1048 between Drosophila Spargel/dPGC-1 and mammalian PGC-1 protein. *Front Genet* 5: 216

1049 Mukherjee S, Duttaroy A (2013) Spargel/dPGC-1 is a new downstream effector in the insulin-TOR
1050 signaling pathway in Drosophila. *Genetics* 195: 433-441

1051 Nagaraj R, Gururaja-Rao S, Jones KT, Slattery M, Negre N, Braas D, Christofk H, White KP, Mann R,
1052 Banerjee U (2012) Control of mitochondrial structure and function by the Yorkie/YAP oncogenic
1053 pathway. *Genes Dev* 26: 2027-2037

1054 Naon D, Hernandez-Alvarez MI, Shinjo S, Wieczor M, Ivanova S, Martins de Brito O, Quintana A,
1055 Hidalgo J, Palacin M, Aparicio P *et al* (2023) Splice variants of mitofusin 2 shape the endoplasmic
1056 reticulum and tether it to mitochondria. *Science* 380: eadh9351

1057 Narendra DP, Jin SM, Tanaka A, Suen DF, Gautier CA, Shen J, Cookson MR, Youle RJ (2010) PINK1 is
1058 selectively stabilized on impaired mitochondria to activate Parkin. *PLoS Biol* 8: e1000298

1059 Nolo R, Morrison CM, Tao C, Zhang X, Halder G (2006) The bantam microRNA is a target of the hippo
1060 tumor-suppressor pathway. *Curr Biol* 16: 1895-1904

1061 Owusu-Ansah E, Yavari A, Mandal S, Banerjee U (2008) Distinct mitochondrial retrograde signals
1062 control the G1-S cell cycle checkpoint. *Nat Genet* 40: 356-361

1063 Panchal K, Tiwari AK (2020) Miro, a Rho GTPase genetically interacts with Alzheimer's disease-
1064 associated genes (Tau, Abeta42 and Appl) in Drosophila melanogaster. *Biol Open* 9

1065 Pavlova NN, Thompson CB (2016) The Emerging Hallmarks of Cancer Metabolism. *Cell Metab* 23:
1066 27-47

1067 Picard M, Shirihai OS, Gentil BJ, Burelle Y (2013) Mitochondrial morphology transitions and
1068 functions: implications for retrograde signaling? *Am J Physiol Regul Integr Comp Physiol* 304: R393-
1069 406

1070 Pinal N, Calleja M, Morata G (2019) Pro-apoptotic and pro-proliferation functions of the JNK
1071 pathway of Drosophila: roles in cell competition, tumorigenesis and regeneration. *Open Biol* 9:
1072 180256

1073 Puigserver P, Wu Z, Park CW, Graves R, Wright M, Spiegelman BM (1998) A cold-inducible
1074 coactivator of nuclear receptors linked to adaptive thermogenesis. *Cell* 92: 829-839

1075 Qian L, Zhu Y, Deng C, Liang Z, Chen J, Chen Y, Wang X, Liu Y, Tian Y, Yang Y (2024) Peroxisome
1076 proliferator-activated receptor gamma coactivator-1 (PGC-1) family in physiological and
1077 pathophysiological process and diseases. *Signal Transduct Target Ther* 9: 50

1078 Qian W, Choi S, Gibson GA, Watkins SC, Bakkenist CJ, Van Houten B (2012) Mitochondrial
1079 hyperfusion induced by loss of the fission protein Drp1 causes ATM-dependent G2/M arrest and
1080 aneuploidy through DNA replication stress. *J Cell Sci* 125: 5745-5757

1081 Rai M, Katti P, Nongthomba U (2014) Drosophila Erect wing (Ewg) controls mitochondrial fusion
1082 during muscle growth and maintenance by regulation of the Opa1-like gene. *J Cell Sci* 127: 191-203

1083 Rera M, Bahadorani S, Cho J, Koehler CL, Ulgherait M, Hur JH, Ansari WS, Lo T, Jr., Jones DL, Walker
1084 DW (2011) Modulation of longevity and tissue homeostasis by the Drosophila PGC-1 homolog. *Cell*
1085 *Metab* 14: 623-634

1086 Rizzuto R, Brini M, Pizzo P, Murgia M, Pozzan T (1995) Chimeric green fluorescent protein as a tool
1087 for visualizing subcellular organelles in living cells. *Curr Biol* 5: 635-642

1088 Rogers RP, Rogina B (2014) Increased mitochondrial biogenesis preserves intestinal stem cell
1089 homeostasis and contributes to longevity in Indy mutant flies. *Aging (Albany NY)* 6: 335-350

1090 Satyanarayana A, Kaldis P (2009) Mammalian cell-cycle regulation: several Cdks, numerous cyclins
1091 and diverse compensatory mechanisms. *Oncogene* 28: 2925-2939

1092 Saxena S, Zou L (2022) Hallmarks of DNA replication stress. *Mol Cell* 82: 2298-2314

1093 Scarpulla RC (2011) Metabolic control of mitochondrial biogenesis through the PGC-1 family
1094 regulatory network. *Biochim Biophys Acta* 1813: 1269-1278

1095 Senft D, Ronai ZA (2016) Regulators of mitochondrial dynamics in cancer. *Curr Opin Cell Biol* 39: 43-
1096 52

1097 Shu Z, Deng WM (2017) Differential Regulation of Cyclin E by Yorkie-Scalloped Signaling in Organ
1098 Development. *G3 (Bethesda)* 7: 1049-1060

1099 Siu KT, Rosner MR, Minella AC (2012) An integrated view of cyclin E function and regulation. *Cell*
1100 *Cycle* 11: 57-64

1101 Song S, Andrejeva D, Freitas FCP, Cohen SM, Herranz H (2019) dTcf/Pangolin suppresses growth and
1102 tumor formation in Drosophila. *Proc Natl Acad Sci U S A* 116: 14055-14064

1103 Sonoda J, Mehl IR, Chong LW, Nofsinger RR, Evans RM (2007) PGC-1beta controls mitochondrial
1104 metabolism to modulate circadian activity, adaptive thermogenesis, and hepatic steatosis. *Proc Natl*
1105 *Acad Sci U S A* 104: 5223-5228

1106 Spruck CH, Won KA, Reed SI (1999) Deregulated cyclin E induces chromosome instability. *Nature*
1107 401: 297-300

1108 Stowers RS, Megeath LJ, Gorska-Andrzejak J, Meinertzhagen IA, Schwarz TL (2002) Axonal transport
1109 of mitochondria to synapses depends on milton, a novel Drosophila protein. *Neuron* 36: 1063-1077

1110 Sullivan LB, Gui DY, Vander Heiden MG (2016) Altered metabolite levels in cancer: implications for
1111 tumour biology and cancer therapy. *Nat Rev Cancer* 16: 680-693

1112 Takata K, Yoshida H, Hirose F, Yamaguchi M, Kai M, Oshige M, Sakimoto I, Koiwai O, Sakaguchi K
1113 (2001) Drosophila mitochondrial transcription factor A: characterization of its cDNA and expression
1114 pattern during development. *Biochem Biophys Res Commun* 287: 474-483

1115 Tan Z, Luo X, Xiao L, Tang M, Bode AM, Dong Z, Cao Y (2016) The Role of PGC1alpha in Cancer
1116 Metabolism and its Therapeutic Implications. *Mol Cancer Ther* 15: 774-782

1117 Tang BL (2015) MIRO GTPases in Mitochondrial Transport, Homeostasis and Pathology. *Cells* 5

1118 Tapon N, Harvey KF, Bell DW, Wahrer DC, Schiripo TA, Haber D, Hariharan IK (2002) salvador
1119 Promotes both cell cycle exit and apoptosis in Drosophila and is mutated in human cancer cell lines.
1120 *Cell* 110: 467-478

1121 Terriente-Felix A, Wilson EL, Whitworth AJ (2020) Drosophila phosphatidylinositol-4 kinase fwd
1122 promotes mitochondrial fission and can suppress Pink1/parkin phenotypes. *PLoS Genet* 16:
1123 e1008844

1124 Thompson BJ, Cohen SM (2006) The Hippo pathway regulates the bantam microRNA to control cell
1125 proliferation and apoptosis in Drosophila. *Cell* 126: 767-774

1126 Tiefenbock SK, Baltzer C, Egli NA, Frei C (2010) The Drosophila PGC-1 homologue Spargel coordinates
1127 mitochondrial activity to insulin signalling. *EMBO J* 29: 171-183

1128 Torrano V, Valcarcel-Jimenez L, Cortazar AR, Liu X, Urosevic J, Castillo-Martin M, Fernandez-Ruiz S,
1129 Morciano G, Caro-Maldonado A, Guiu M *et al* (2016) The metabolic co-regulator PGC1alpha
1130 suppresses prostate cancer metastasis. *Nat Cell Biol* 18: 645-656

1131 Tubbs A, Nussenzweig A (2017) Endogenous DNA Damage as a Source of Genomic Instability in
1132 Cancer. *Cell* 168: 644-656

1133 Uhlirova M, Bohmann D (2006) JNK- and Fos-regulated Mmp1 expression cooperates with Ras to
1134 induce invasive tumors in Drosophila. *EMBO J* 25: 5294-5304

1135 Vianna CR, Huntgeburth M, Coppari R, Choi CS, Lin J, Krauss S, Barbatelli G, Tzameli I, Kim YB, Cinti
1136 S *et al* (2006) Hypomorphic mutation of PGC-1beta causes mitochondrial dysfunction and liver
1137 insulin resistance. *Cell Metab* 4: 453-464

1138 Villena JA (2015) New insights into PGC-1 coactivators: redefining their role in the regulation of
1139 mitochondrial function and beyond. *FEBS J* 282: 647-672

1140 Vincow ES, Merrihew G, Thomas RE, Shulman NJ, Beyer RP, MacCoss MJ, Pallanck LJ (2013) The
1141 PINK1-Parkin pathway promotes both mitophagy and selective respiratory chain turnover in vivo.
1142 *Proc Natl Acad Sci U S A* 110: 6400-6405

1143 Vyas S, Zaganjor E, Haigis MC (2016) Mitochondria and Cancer. *Cell* 166: 555-566

1144 Wang Y, Peng J, Yang D, Xing Z, Jiang B, Ding X, Jiang C, Ouyang B, Su L (2024) From metabolism to
1145 malignancy: the multifaceted role of PGC1alpha in cancer. *Front Oncol* 14: 1383809

1146 Watkins G, Douglas-Jones A, Mansel RE, Jiang WG (2004) The localisation and reduction of nuclear
1147 staining of PPARgamma and PGC-1 in human breast cancer. *Oncol Rep* 12: 483-488

1148 Wu Z, Puigserver P, Andersson U, Zhang C, Adelmant G, Mootha V, Troy A, Cinti S, Lowell B, Scarpulla
1149 RC *et al* (1999) Mechanisms controlling mitochondrial biogenesis and respiration through the
1150 thermogenic coactivator PGC-1. *Cell* 98: 115-124

1151 Yao CH, Wang R, Wang Y, Kung CP, Weber JD, Patti GJ (2019) Mitochondrial fusion supports
1152 increased oxidative phosphorylation during cell proliferation. *Elife* 8

1153 Yu K, Ramkumar N, Wong KKL, Tettweiler G, Verheyen EM (2023) The AMPK-like protein kinases
1154 Sik2 and Sik3 interact with Hipk and induce synergistic tumorigenesis in a Drosophila cancer model.
1155 *Front Cell Dev Biol* 11: 1214539

1156 Zhang Y, Ba Y, Liu C, Sun G, Ding L, Gao S, Hao J, Yu Z, Zhang J, Zen K *et al* (2007) PGC-1alpha induces
1157 apoptosis in human epithelial ovarian cancer cells through a PPARgamma-dependent pathway. *Cell*
1158 *Res* 17: 363-373

1159 Zheng Y, Pan D (2019) The Hippo Signaling Pathway in Development and Disease. *Dev Cell* 50: 264-
1160 282

1161 Zorzano A, Liesa M, Sebastian D, Segales J, Palacin M (2010) Mitochondrial fusion proteins: dual
1162 regulators of morphology and metabolism. *Semin Cell Dev Biol* 21: 566-574

1163

1164

FIGURES

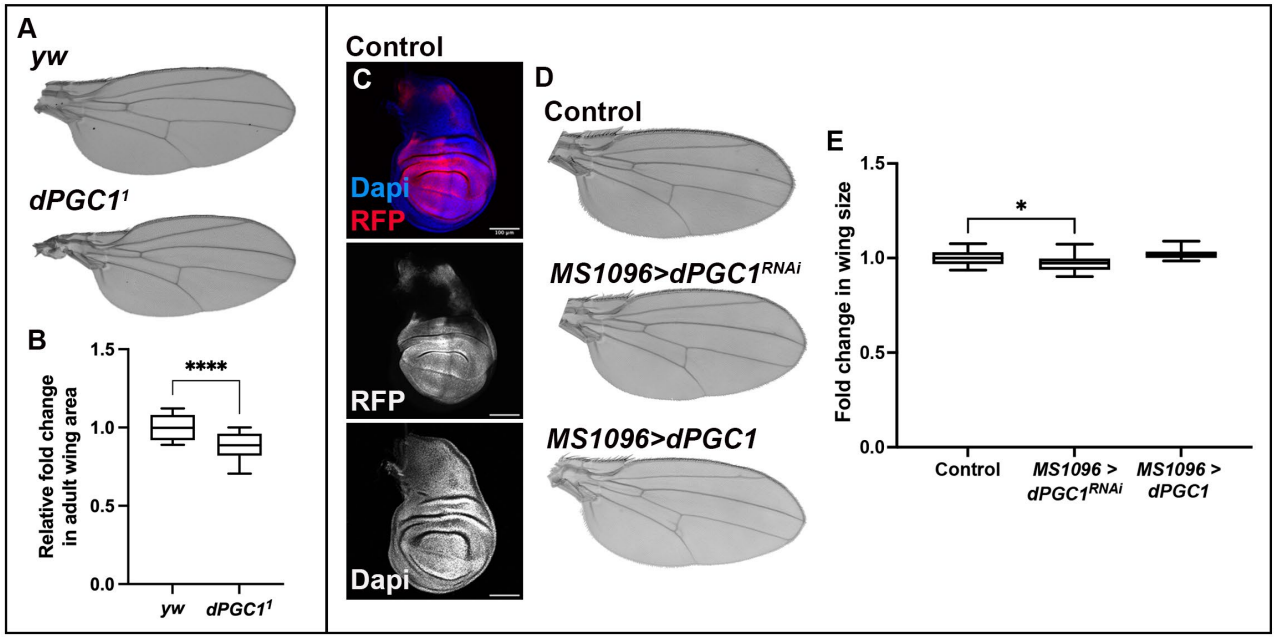

Figure 1. Reduced dPGC1 Activity Leads to Smaller Wings

(A) Cuticle preparations of adult wings from the following genotypes: *yw/yw* (control) and *dPGC1¹/dPGC1¹* (mutant).

(B) Quantification of adult wing size of the genotypes indicated in A. Wing area is normalized to the mean of the control (*yw*). Statistical significance was determined using an unpaired t-test (n = 20 [*yw*], n = 20 [*dPGC1¹*]). ****, $p < 0.0001$.

(C) Confocal micrograph showing a *MS1096-Gal4, UAS-RFP* third instar wing imaginal disc. RFP labels the region of the disc expressing this Gal4 line and is shown in red. DAPI labels the DNA and is shown in blue. Scale bar, 100 μm.

(D) Cuticle preparations of adult wings from *MS1096-Gal4, UAS-LacZ* control flies; *MS1096-Gal4, UAS-dPGC1-RNAi* flies; and *MS1096-Gal4, EP-dPGC1* flies.

(E) Quantification of adult wing size of the genotypes indicated in D. Wing area is normalized to the mean of the control (*MS1096>LacZ*). Statistical significance was determined using unpaired t-tests with Welch's correction (n = 20 [*MS1096>LacZ*], n = 20 [*MS1096>dPGC1-RNAi*], n = 20 [*MS1096>dPGC1*]). *$p < 0.05$.

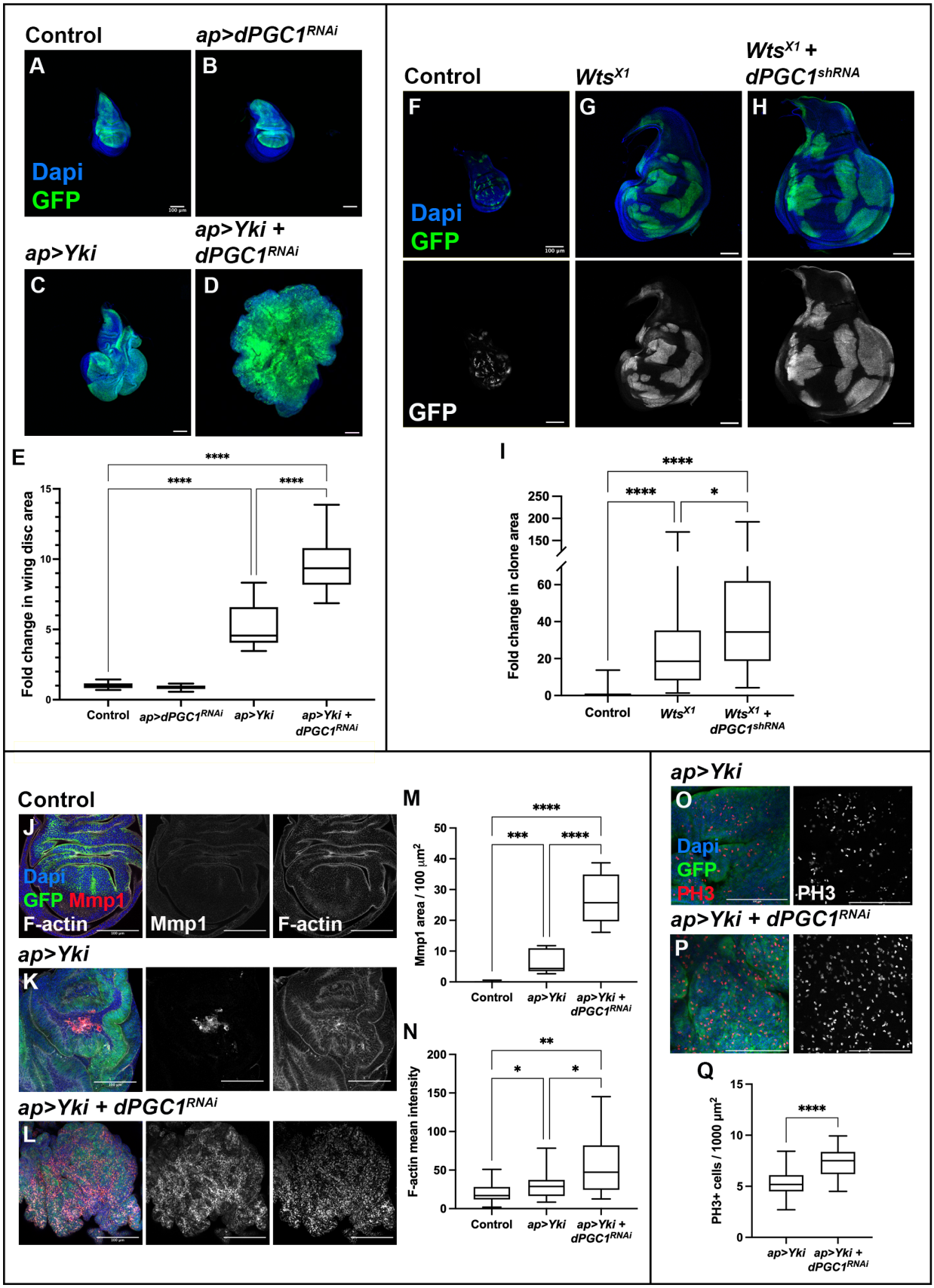

1182

1183 **Figure 2. Oncogenic Growth in Discs Overexpressing *Yki* and Downregulating *dPGC1***

1184 **(A-D)** Confocal micrographs showing discs of the following genotypes: *ap-Gal4, UAS-GFP, UAS-*
1185 *LacZ* (A); *ap-Gal4, UAS-GFP, UAS-dPGC1-RNAi* (B); *ap-Gal4, UAS-GFP, UAS-Yki, UAS-LacZ* (C);
1186 and *ap-Gal4, UAS-GFP, UAS-Yki, UAS-dPGC1-RNAi* (D). GFP is shown in green, and DAPI labels
1187 the DNA and is shown in blue. Scale bars, 100 μm.

1188 **(E)** Quantification of GFP-positive area in third instar wing imaginal discs of the genotypes shown in
1189 A-D. GFP-positive area is normalized to the mean of the control *(ap>LacZ*). Statistical significance
1190 was determined using unpaired t-tests with Welch's correction (n = 18 [*ap>LacZ*], n = 19 [*ap>dPGC1-*
1191 *RNAi*], n = 20 [*ap>Yki*], n = 20 *[ap>Yki, dPGC1-RNAi*]). ****p < 0.0001.

1192 **(F-H)** Confocal micrographs showing representative images of imaginal discs with GFP-labeled
1193 MARCM control clones (F), Wts^{X1} clones (G), and Wts^{X1} clones expressing *UAS-dPGC1-shRNA* (H).
1194 GFP is shown in green, and DAPI labels the DNA and is shown in blue. Scale bars, 100 μm.

1195 **(I)** Quantification of GFP-positive clones in the genotypes shown in F-H. GFP-positive area is
1196 normalized to the mean of the control. Statistical significance was determined using a Kruskal Wallis
1197 test for non-parametric data (n = 102 [Control], n = 92 [Wts^{X1}], n = 65 [Wts^{X1} + $dPGC1^{shRNA}$]). *p <
1198 0.05, ****p < 0.0001.

1199 (**J-L**) Confocal micrographs of imaginal wing discs of the following genotypes: *ap-Gal4, UAS-GFP,*
1200 *UAS-LacZ* (J); *ap-Gal4, UAS-GFP, UAS-Yki, UAS-LacZ* (K); and *ap-Gal4, UAS-GFP, UAS-Yki,*
1201 *UAS-dPGC1-RNAi* (L). F-actin labels cell polarity and is shown in grayscale. Mmp1 is shown in red.
1202 GFP is shown in green. DAPI labels the DNA and is shown in blue. Scale bars, 100 μm.

1203 (**M**) Quantification of Mmp1 area per GFP-positive area in the genotypes shown in J-L. Statistical
1204 significance was determined using a Brown-Forsythe and Welch ANOVA test (n = 12 [*ap>LacZ*], n
1205 = 11 [*ap>Yki*], n = 11 *[ap>Yki, dPGC1-RNAi*]). ***p < 0.001, ****p < 0.0001.

1206 (**N**) Quantification of F-actin mean intensity in the genotypes shown in J-L. Statistical significance
1207 was determined using a Brown-Forsythe and Welch ANOVA test (n = 31 [*ap>LacZ*], n = 22 [*ap>Yki*],
1208 n = 19 [*ap>Yki, dPGC1-RNAi*]). *p < 0.05, **p < 0.01.

1209 (**O, P**) Confocal micrographs showing magnifications from tumorous wing discs with the following
1210 genotypes: *ap-Gal4, UAS-Yki, UAS-GFP, UAS-LacZ* (O) and *ap-Gal4, UAS-Yki, UAS-GFP, UAS-*
1211 *dPGC1-RNAi* (P). PH3 labels mitotic cells and is shown in red. GFP is shown in green. DAPI labels
1212 the DNA and is shown in blue. Scale bars, 10 μm.

1213 (**Q**) Quantification of number of PH3-positive cells per GFP-positive area in the genotypes shown in
1214 O and P. Statistical significance was determined using an unpaired t-test (n = 23 [*ap>Yki*], n = 19
1215 *[ap>Yki, dPGC1-RNAi*]). ****p < 0.0001.

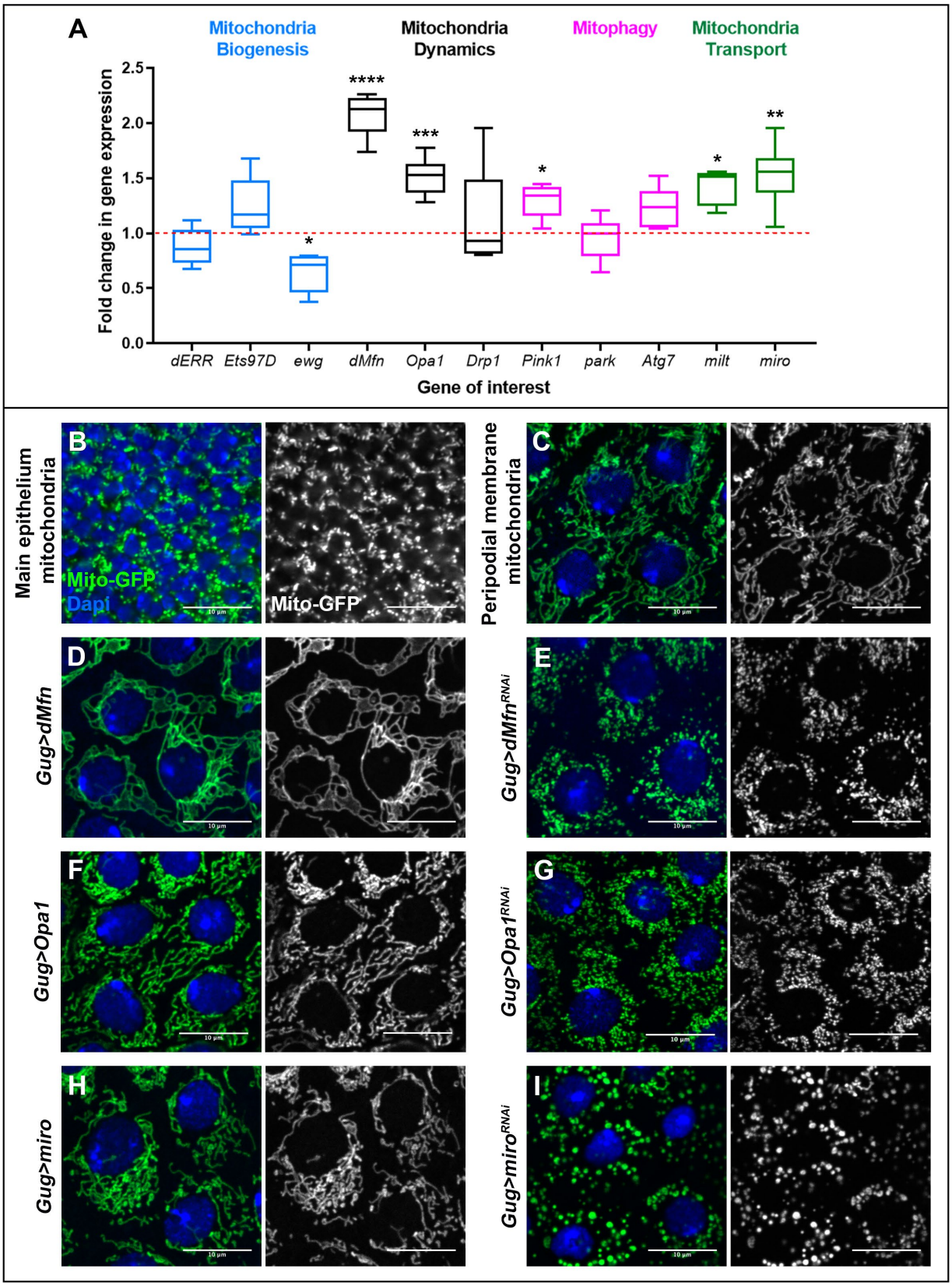

1216

1217 **Figure 3. Aberrant Mitochondrial Dynamics in *Yki* + *dPGC1-RNAi* Tumorous Discs**

1218 **(A)** mRNA quantification by qPCR of the indicated genes in *ap-Gal4, UAS-GFP, UAS-Yki, UAS-*
1219 *dPGC1-RNAi* wing imaginal discs using *ap-Gal4, UAS-GFP, UAS-Yki, UAS-LacZ* as the control
1220 genotype. Genes are separated in different categories: mitochondria biogenesis (blue), mitochondria
1221 dynamics (black), mitophagy (pink), and mitochondria transport (green). Each genotype was run in
1222 five to six biological replicates. RP49 was used as the housekeeping gene. Statistical significance
1223 was determined using unpaired t-tests with Welch's correction for parametric data and Mann-
1224 Whitney tests for non-parametric data. *$p < 0.05$, **$p < 0.01$, ***$p < 0.001$, ****$p < 0.0001$.

1225 **(B)** Confocal micrograph of the main epithelium of an *ap-Gal4, UAS-Mito-GFP* wing imaginal disc.
1226 Mitochondria are labeled with Mito-GFP and are shown in green. DAPI is shown in blue. Scale bar,
1227 10 μm.

1228 **(C)** Confocal micrograph of the peripodial membrane of a *Gug-Gal4, UAS-Mito-GFP* wing imaginal
1229 disc. Mitochondria are labeled with Mito-GFP and are shown in green. DAPI is shown in blue. Scale
1230 bar, 10 μm.

1231 **(D-I)** Confocal micrographs of the peripodial membrane in the following genotypes: *Gug-Gal4, UAS-*
1232 *Mito-GFP, UAS-dMfn* (D); *Gug-Gal4, UAS-Mito-GFP, UAS-dMfn-RNAi* (E); *Gug-Gal4, UAS-Mito-*
1233 *GFP, EP-Opa1* (F); *Gug-Gal4, UAS-Mito-GFP, UAS-Opa1-RNAi* (G); *Gug-Gal4, UAS-Mito-GFP,*
1234 *UAS-miro* (H); and *Gug-Gal4, UAS-Mito-GFP, UAS-miro-RNAi* (I). Mitochondria are labeled with
1235 Mito-GFP and are shown in green. DAPI is shown in blue. Scale bars, 10 μm.

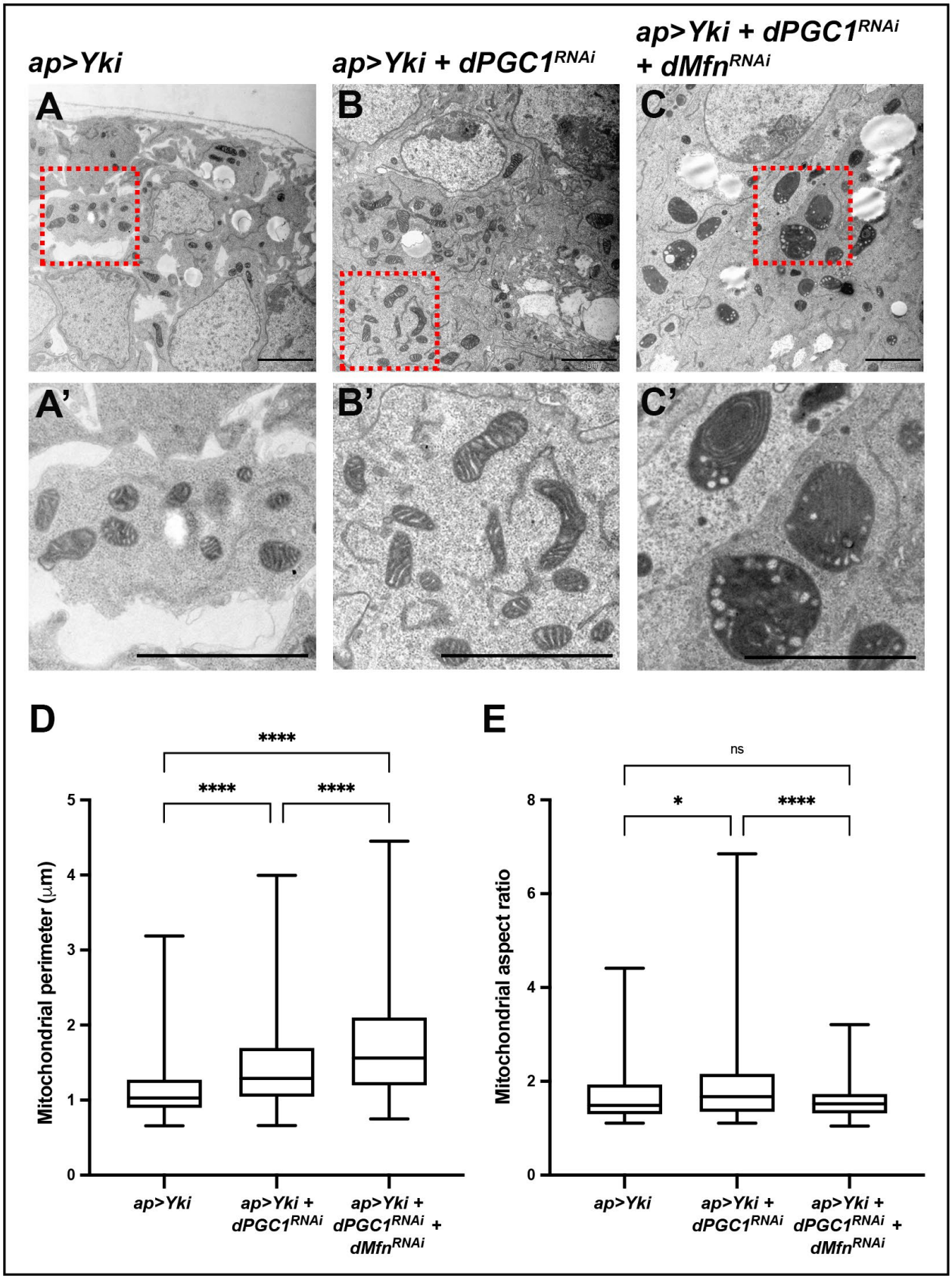

1236

1237 **Figure 4. dPGC1 and dMfn Regulate Mitochondrial Morphology in Yki-Driven Tumors**

1238 **(A-C)** Representative electron microscopy micrographs obtained from discs of the following
1239 genotypes: *ap-Gal4, UAS-GFP, UAS-Yki, UAS-LacZ* (A); *ap-Gal4, UAS-GFP, UAS-Yki, UAS-*
1240 *dPGC1-RNAi* (B); and *ap-Gal4, UAS-GFP, UAS-Yki, UAS-dPGC1-RNAi, UAS-dMfn-RNAi* (C). The
1241 dashed red squares in A-C indicate the regions that are shown as magnifications in A'-C'. Scale
1242 bars, 2 μm.

1243 **(D, E)** Quantification of mitochondrial perimeter (D) and mitochondrial aspect ratio (E) in the
1244 genotypes shown in A-C. Statistical significance was determined using one-way ANOVA tests (n =
1245 164 [*ap>Yki*], n = 214 [*ap>Yki, dPGC1-RNAi*], n = 218 [*ap>Yki, dPGC1-RNAi, dMfn-RNAi*]). ns, non-
1246 significant. *$p < 0.05$, ****$p < 0.0001$.

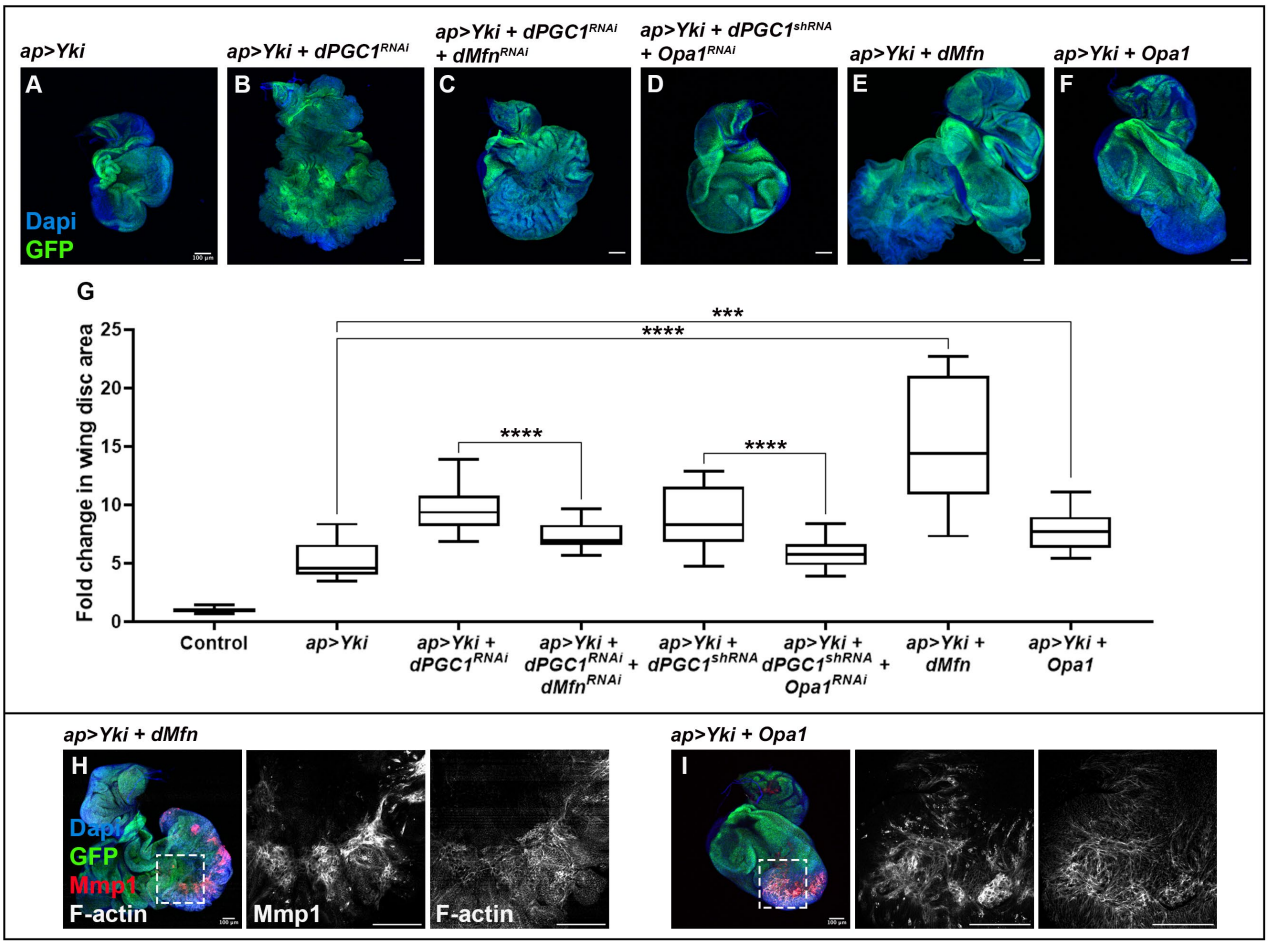

Figure 5. dMfn and Opa1 Synergize with Yki to Promote Tumor Growth and Malignancy

(A-F) Confocal micrographs showing discs of the following genotypes: *ap-Gal4, UAS-GFP, UAS-Yki, UAS-LacZ* (A); *ap-Gal4, UAS-GFP, UAS-Yki, UAS-dPGC1-RNAi* (B); *ap-Gal4, UAS-GFP, UAS-Yki, UAS-dPGC1-RNAi, UAS-dMfn-RNAi* (C); *ap-Gal4, UAS-GFP, UAS-Yki, UAS-dPGC1-shRNA, UAS-Opa1-RNAi* (D); *ap-Gal4, UAS-GFP, UAS-Yki, UAS-dMfn* (E); and *ap-Gal4, UAS-GFP, UAS-Yki, EP-Opa1* (F). GFP is shown in green, and DAPI labels the DNA and is shown in blue. Scale bars, 100 μm.

(G) Quantification of GFP-positive area in third instar wing imaginal discs of the genotypes shown in A-F. GFP-positive areas are normalized to the mean of the control (*ap>LacZ*). Statistical significance was determined using unpaired t-tests with Welch's correction (n = 18 [*ap>LacZ*], n = 20 [*ap>Yki*], n = 20 [*ap>Yki, dPGC1-RNAi*], n = 20 [*ap>Yki, dPGC1-RNAi, dMfn-RNAi*], n = 20 [*ap>Yki, dPGC1-shRNA*], n = 20 [*ap>Yki, dPGC1-shRNA, Opa1-RNAi*], n = 13 [*ap>Yki, dMfn*], n = 12 [*ap>Yki, Opa1*]). ***$p < 0.001$, ****$p < 0.0001$.

(H, I) Confocal micrographs of imaginal discs of the following genotypes: *ap-Gal4, UAS-GFP, UAS-Yki, UAS-dMfn* (H) and *ap-Gal4, UAS-GFP, UAS-Yki, UAS-Opa1* (I). F-actin labels cell polarity and epithelial organization and is shown in grayscale. Mmp1 is shown in red. GFP is shown in green. DAPI labels the DNA and is shown in blue. Scale bars, 100 μm.

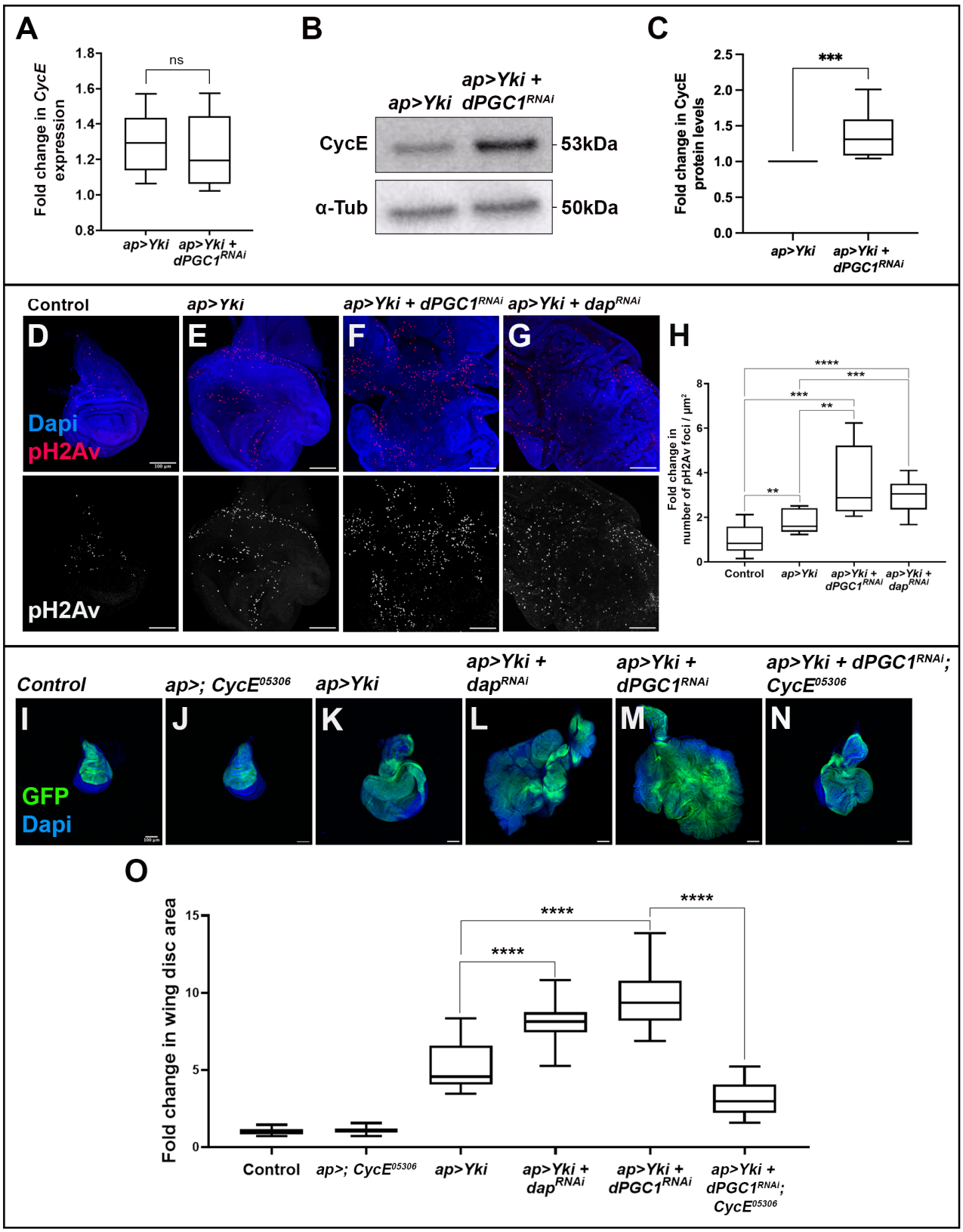

Figure 6. Cyclin E Stabilization Drives Tumor Growth and DNA Damage in *Yki + dPGC1-RNAi* Discs

1268 **(A)** Quantification of *Cyclin E* mRNA by qPCR in imaginal discs of the following genotypes: *ap-Gal4,*
1269 *UAS-GFP, UAS-Yki, UAS-LacZ* (*ap>Yki*) and *ap-Gal4, UAS-GFP, UAS-Yki, UAS-dPGC1-RNAi*
1270 (*ap>Yki, dPGC1-RNAi*). Each genotype was run in four to five biological replicates. RP49 was used
1271 as the housekeeping gene. Statistical significance was determined using an unpaired t-test with
1272 Welch's correction. ns, non-significant.

1273 **(B)** Western blot showing Cyclin E protein levels in third instar wing imaginal discs of the indicated
1274 genotypes. α-Tubulin was used as the loading control.

1275 (**C**) Relative quantification of Cyclin E protein levels in wing imaginal discs of the genotypes shown
1276 in B. Cyclin E protein levels were normalized to α-Tubulin protein levels for each western blot
1277 membrane. The obtained Cyclin E/α-Tubulin ratio was normalized to that of the control (*ap>Yki*).
1278 Statistical significance was determined using a Mann-Whitney test (n = 7). ***p < 0.001.

1279 **(D-G)** Maximum projection of confocal micrographs of imaginal discs of the following genotypes: *ap-*
1280 *Gal4, UAS-GFP, UAS-LacZ* (D); *ap-Gal4, UAS-GFP, UAS-Yki, UAS-LacZ* (E); *ap-Gal4, UAS-GFP,*
1281 *UAS-Yki, UAS-dPGC1-RNAi* (F); and *ap-Gal4, UAS-GFP, UAS-Yki, UAS-dap-RNAi* (G). pH2Av is
1282 shown in red, and DAPI is shown in blue. Scale bars, 100 μm.

1283 **(H)** Quantification of pH2Av-positive foci in the genotypes shown in D-G. Data was normalized to the
1284 mean of the control (*ap>LacZ*). Statistical significance was determined using unpaired t-tests with
1285 Welch's correction (n = 12 [*ap>LacZ*], n = 12 [*ap>Yki*], n = 12 [*ap>Yki, dPGC1-RNAi*], n = 20 [*ap>Yki,*
1286 *dap-RNAi*]). **p < 0.01, **p < 0.001, ****p < 0.0001.

1287 **(I-N)** Confocal micrographs showing discs of the following genotypes: *ap-Gal4, UAS-GFP, UAS-*
1288 *LacZ* (I); *ap-Gal4, UAS-GFP/Cyclin E-05306* (J); *ap-Gal4, UAS-GFP, UAS-Yki, UAS-LacZ* (K); *ap-*
1289 *Gal4, UAS-GFP, UAS-Yki, UAS-dap-RNAi* (L), *ap-Gal4, UAS-GFP, UAS-Yki, UAS-dPGC1-RNAi*
1290 (M); and *ap-Gal4, UAS-GFP, UAS-Yki, UAS-dPGC1-RNAi/Cyclin E-05306* (N). GFP is shown in
1291 green, and DAPI labels the DNA and is shown in blue. Scale bars, 100 μm.

1292 **(O)** Quantification of GFP-positive area in third instar wing imaginal discs of the genotypes shown in
1293 I-N. GFP-positive area is normalized to the mean of the control (*ap>LacZ*). Statistical significance
1294 was determined using unpaired t-tests with Welch's correction (n = 18 [*ap>LacZ*], n = 20 [*ap>; CycE-*
1295 *05306*], n = 20 [*ap>Yki*], n = 20 [*ap>Yki, dap-RNAi*] n = 20 [*ap>Yki, dPGC1-RNAi*], n = 20 [*ap>Yki,*
1296 *dPGC1-RNAi; CycE-05306*]). ****p < 0.0001.